

Contents

6 Radio AGN in the Boötes field:	1
6.1 Introduction	2
6.2 Radio Data	3
6.3 Multiwavelength Data	4
6.3.1 Combined Photometry Catalogue	4
6.3.2 Additional Multiwavelength Surveys	5
6.3.3 The AGN and Galaxy Evolution Survey	6
6.4 SED fitting	6
6.4.1 Photometric Redshifts	6
6.4.2 Stellar Masses, Star Formation Rates and Rest-frame Colours	9
6.5 Optical identification of Radio Sources	11
6.5.1 Visual Classification	11
6.5.2 Likelihood Ratio	11
6.5.3 Match Results	12
6.5.4 Contamination	13
6.6 Properties of Radio Sources	15
6.6.1 Local Reference Sample	15
6.6.2 Subsample Selection	16
6.6.3 IR SED fitting	16
6.6.4 Star Formation contribution	19
6.6.5 Colour-mass distribution	19
6.6.6 Radio-loud fraction	21
6.7 Conclusion	27
6.7.1 Future work	29
6.A Radio-Optical Matches	29
6.B Example SED fits	34
Bibliography	39

Contents

Radio AGN in the Boötes field:

This paper presents a study of the redshift evolution of radio-loud active galactic nuclei (AGN) as a function of the properties of their galaxy hosts in the Boötes field. To achieve this we produce a catalogue of galaxies for which we derive photometric redshifts, stellar masses and rest-frame colours. The galaxies are matched to low frequency radio sources from 150 MHz LOFAR observations. From the matched radio-optical catalogues, we select a subsample of 974 high power $P_{1.4 \text{ GHz}} > 10^{25} \text{ W Hz}^{-1}$ radio sources between $0.5 \leq z < 2$. We present further spectral energy distribution (SED) fitting to determine the mid-infrared AGN contribution for the radio-sources and use this information to classify them as High versus Low Excitation Radio Galaxies (HERGs and LERGs). We study the radio-loud fraction for HERGs and LERGs as a function of stellar mass and host galaxy colour. The fraction of HERGs increases with redshift. The fraction of sources in blue galaxies increases with redshift, while that in red galaxies decreases.

Williams, W. L., Röttgering, H. J. A., Rigby, E. E., and Calistro Rivera, G.
in preparation

6.1 Introduction

The growth and evolution of black holes plays a significant role in the framework of galaxy evolution. It is important then to understand the fueling mechanisms of Active Galactic Nuclei (AGN) and their ‘feedback’ processes by which the central black holes can control or terminate star formation in their host galaxies (see e.g. Best et al. 2006, 2007; Bower et al. 2006; Croton et al. 2006; Fabian et al. 2006; Cattaneo et al. 2009). From studies of radio-loud AGN, which are identified by their synchrotron emission for the jets, it has become clear that there are two classes of these sources distinguished by their Eddington-scaled accretion rates (Best & Heckman 2012; Son et al. 2012; Russell et al. 2013; Mingo et al. 2014; Gürkan et al. 2014; Fernandes et al. 2015). The first population of RL AGN is associated with radiatively efficient accretion via an accretion disc (e.g. Shakura & Sunyaev 1973). These sources fit the paradigm of classic optical ‘quasars’ (Silk & Rees 1998), radiating across the electromagnetic spectrum (e.g. Barthel 1989; Antonucci 1993; Urry & Padovani 1995). This ‘cold mode’ or ‘radiative mode’ is characterised by strong optical emission lines and so are referred to as ‘high-excitation’ sources. It has been found that high excitation radio galaxies (HERGs) are typically hosted by lower mass, bluer galaxies in less dense environments (e.g. Tasse et al. 2008b; Janssen et al. 2012). This mode may be important in curtailing star formation at high redshift and setting up the tight black hole vs bulge mass relation observed in the nearby Universe (Magorrian et al. 1998). The second class of radio galaxies was first noted by their lack of emission lines (Hine & Longair 1979; Laing et al. 1994; Jackson & Rawlings 1997) and are thought to occur when hot gas accretes directly onto the supermassive black hole in a radiatively inefficient manner (Hardcastle et al. 2007) through advection dominated accretion flows (ADAFs, e.g. Narayan & Yi 1995). They also lack any evidence of mid-infrared emission from dusty tori (Whysong & Antonucci 2004; Ogle et al. 2006) and accretion-related X-ray emission (Hardcastle et al. 2006; Evans et al. 2006). These low excitation radio galaxies (LERGs) are hosted by fundamentally different galaxies: higher mass, redder and occurring in more dense environments (Best et al. 2005a). This ‘radio mode’, ‘hot mode’ or ‘jet mode’ in particular provides a direct feedback connection between the AGN and its hot gas fuel supply in the manner of work done by the expanding radio lobes on the hot intra-cluster gas. It may be responsible for maintaining elliptical galaxies at lower redshifts as ‘old, red and dead’ (e.g. Best et al. 2006) and for preventing strong cooling flows in galaxy clusters (e.g. Fabian et al. 2006). For a comprehensive review on the current understanding of the HERG/LERG dichotomy see Heckman & Best (2014) and McNamara & Nulsen (2012) and references therein.

In order to understand the relative significance of the different types of radio-AGN feedback we need to understand the cosmic evolution of radio sources in detail. It is also well known that, within the local universe ($z \lesssim 0.3$), the fraction of galaxies which host a radio source, i.e. the radio-loud fraction, is a very steep function of host galaxy stellar mass ($f_{\text{radio-loud}} \propto M_*^{2.5}$, Best et al. 2005b; Janssen et al. 2012), increasing to > 30 per cent at stellar masses above $5 \times 10^{11} M_\odot$ for radio luminosities $> 10^{23} \text{ W Hz}^{-1}$. At these redshifts the radio-loud AGN population is dominated by LERGs (Best et al. 2006) so when the radio-loud fraction for HERGs is considered separately, the mass-dependence is much shallower, $f_{\text{radio-loud}} \propto M_*^{1.5}$ (Janssen et al. 2012). Furthermore, the fraction of radio-loud AGN for the two classes have different relationships with radio luminosity, galaxy color and star formation rate. Red (passive) galaxies are a factor of a few times more likely to host LERGs than blue (star-forming) galaxies of the same stellar mass. Blue galaxies show a higher probability of hosting HERGs at all radio luminosities. Moreover,

for blue galaxies, the likelihood of hosting any radio AGN is a strong positive function of the SFR. The presence of cold, star-forming gas in a galaxy clearly enhances the probability of its central BH becoming a radio-loud AGN. This means that LERG activity, especially at high radio luminosities, is not solely related to hot halo gas accretion (Heckman & Best 2014). In studying the radio-loud fraction at $z \sim 1 - 2$, Williams & Röttgering (2015) found more than an order of magnitude difference in the fraction of lower mass galaxies ($M_* < 10^{10.75} M_\odot$) which host radio-loud AGN with radio powers $P_{1.4\text{GHz}} > 10^{24} \text{W Hz}^{-1}$. The key open question is how the radio loud fraction, and radio source duty cycle, depend on host galaxy masses and colours for HERGs and LERGs at higher redshifts.

The main distinguishing point between HERGs and LERGs is their optical spectra. Best et al. (2014) provide the largest sample of intermediate redshift ($z < 1$) that is spectroscopically classified into jet- and radiative mode AGN. In order to pursue studies with large samples at higher redshift a method is needed that does not require spectroscopy. Mid-infrared (MIR) quasar-selection techniques (Stern et al. 2005; Donley et al. 2012; Stern et al. 2012) are insufficient as they do not select all high excitation sources. Neither does selecting on X-ray emission alone (e.g. Hickox et al. 2009). Using high power sources out to $z \approx 4$, all of which have optical spectroscopy, Gürkan et al. (2014) have recently suggested that there is a clear division between LERGs and HERGs in the mid-IR-radio plane and a simple cut in $22 \mu\text{m}$ luminosity can separate the populations. In this paper we attempt to classify a sample of radio-loud AGN as HERGs and LERGs based on fits to their broad-band spectral energy distributions (SEDs), and use this to study the radio-loud fraction for the two populations between $0.5 \leq z < 2$.

This paper is structured as follows: The LOFAR 150 MHz radio data is described in Section 6.2 and the multiwavelength datasets and catalogues we use are described in Section 6.3. In Section 6.4 we use SED fitting to determine photometric redshifts and galaxy parameters for the sample of optical galaxies. Section 6.5 describes our method for identifying optical counterparts to the LOFAR radio sources. Section 6.6 describes the selection of a well-defined sub-sample of radio-loud AGN and further SED fitting to classify sources from this radio-loud AGN sample as HERGs and LERGs. Throughout this paper we use Vega magnitudes and a concordance cosmology with $\Omega_M = 0.3$, $\Omega_\Lambda = 0.7$, and $H_0 = 70 \text{ km s}^{-1} \text{Mpc}^{-1}$. The spectral index, α , is defined as $S_\nu \propto \nu^\alpha$, where S is the source flux density and ν is the observing frequency. We assume a spectral index of -0.8 unless otherwise stated.

6.2 Radio Data

We use the radio data described by Williams et al. (2015, submitted). The 8 hr observation was taken with the LOw Frequency ARray (LOFAR; van Haarlem et al. 2013) using the High Band Antennae (HBA) and covering the frequency range 130–169 MHz, with a central frequency of ≈ 150 MHz. Particular care was taken in the calibration and imaging to correct for direction-dependent effects (DDEs) caused by the ionosphere and imperfect knowledge of the LOFAR station beam shapes. This DDE calibration and imaging was achieved with the ‘Facet’ calibration scheme presented by van Weeren (prep, submitted). The resulting image covers 19 deg^2 , with an rms noise of $\approx 120 - 150 \mu\text{Jy beam}^{-1}$. Assuming a spectral index of -0.8 , the sensitivity of this map is comparable to the $28 \mu\text{Jy beam}^{-1}$ rms of the WSRT, 1.4 GHz, image made by de Vries et al. (2002). However, the LOFAR resolution of $5.6 \times 7.4''$, compared to $13 \times 27''$ at 1.4 GHz, combined with its positional accuracy of $< 1''$ makes it significantly better for the

6 Radio AGN in the Boötes field:

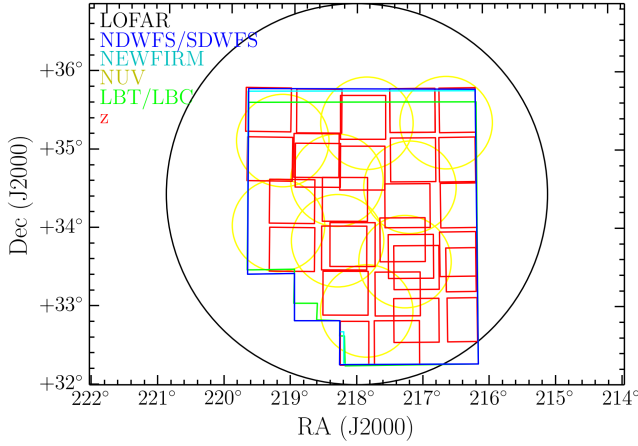


Figure 6.1: Coverage diagram for the Boötes field. The black circle shows the LOFAR 150 MHz coverage. The blue polygon shows the main I -selected psf-matched catalogue region, which is covered completely by both the NDWFS ($B_W RIK$) and SDWFS (3.6, 4.5, 5.8, and 8.0 μm). It covers a total of 9.1 deg^2 , when regions contaminated by bright stars are excluded. The red squares show the z Boötes coverage, which has some gaps. The yellow circles show the GALEX NUV coverage. There is a small area not covered by the NEWFIRM survey (J , H , and K_s , shown in cyan) and the LBT/LBC survey (U_{spec} , and Y , shown in light green).

optical identification of the radio sources. The LOFAR 150 MHz radio source catalogue contains 5 652 sources detected with a peak flux density threshold of 5σ , where σ is the local rms noise. The radio coverage is shown as a circle in Fig. 6.1.

6.3 Multiwavelength Data

The Boötes field is one of the widest of the famous deep extragalactic fields and was originally targeted as one of two fields within the National Optical Astronomy Observatory (NOAO) Deep Wide Field Survey (NDWFS; Jannuzi et al. 1999). Since then it has been surveyed across the electromagnetic spectrum. We describe here the surveys and datasets that are used in this work.

6.3.1 Combined Photometry Catalogue

The primary catalogue that we make use of is the combined I -band-selected psf-matched photometry catalogue presented by Brown et al. (2007, 2008). This catalogue includes 15 bands spanning 0.14–24 μm and combines several different surveys. We describe here briefly the data sets that are included in this catalogue.

The NDWFS included observations in the optical (B_W , R , and I) and the NIR (K) bands. The areal coverage in these four bands is $\approx 9.3 \text{ deg}^2$. The photometry catalogue is based on the third NDWFS data release¹. The B_W , R , I , and K -band images reach depths of 26.7, 25.5,

¹Available from the NOAO Science Archive at <http://www.archive.noao.edu/ndwfs/>.

24.9, and 18.6 mag (5σ within a 2 " diameter aperture) and with an absolute positional uncertainty of the sources of < 0.1 ". The *Spitzer* Deep, Wide-field Survey (SDWFS; Ashby et al. 2009) is a four-epoch MIR survey covering 10 deg² using the InfraRed Array Camera (IRAC) instrument on the *Spitzer* Space Telescope, which provides images at 3.6, 4.5, 5.8, and 8.0 μ m. The average 5σ , 4 "-diameter, aperture-corrected limits are 19.77, 18.83, 16.50, and 15.82 mag at 3.6, 4.5, 5.8, and 8.0 μ m respectively. The Multiband Imaging Photometer (MIPS) AGN and Galaxy Evolution Survey (MAGES; Jannuzi et al. 2010) provided 24 μ m images from *Spitzer*. Further and deeper NIR imaging comes from the NOAO Extremely Wide-Field Infrared Imager (NEWFIRM; Autry et al. 2003) survey¹, which provides J , H and K_s imaging down to a 5σ depth of approximately $J = 22$, $H = 20.8$, $K_s = 19.5$ mag within a 3 " diameter aperture. z -band photometric imaging covering 7.62 deg² comes from the zBoötes survey (Cool 2007), which was performed with the 90Prime wide-field imager (Williams et al. 2004) at prime focus on the Bok 2.3 m Telescope located on Kitt Peak. There are some gaps in the coverage of the Boötes field (see Fig. 6.1) resulting from the 10 ' gaps in the instrument CCDs. The zBoötes survey is complete (at the 50 per cent level) to 22.7 mag over 50 per cent of the field. Bian et al. (2013) have performed a survey using the Large Binocular Camera (LBC) mounted on the 2 \times 8.4 m Large Binocular Telescope (LBT) in binocular mode, which provides imaging in the U_{spec} ($\lambda_0 = 3590\text{\AA}$, FWHM = 540 \AA), and Y -bands ($\lambda_0 = 9840\text{\AA}$, FWHM = 420 \AA) covering 9 deg². They give a 5σ depth in the U_{spec} -band of 25.5 mag. Finally, there is UV coverage of the Boötes field from GALEX/GR6 (Martin et al. 2003; Bianchi et al. 2014) which includes NUV (1800–2750 \AA) and FUV (1400–1700 \AA) imaging. The FUV coverage, however, is limited (< 25 per cent) so we exclude it in later analysis.

Brown et al. (2007) have constructed a combined psf-matched catalogue by regridding and smoothing the individual released survey images to a common scale so that the stellar point-spread function (PSF) is a Moffat profile with a full width at half-maximum (FWHM) of 1.35 " and $\beta = 2.5$ for the B_w -, R -, I -, Y -, H , K -, and K_s -bands and with a FWHM of 1.6 " for the u -, z - and J -bands. PSF fluxes are extracted from these images for all the sources in the I -band using SExtractor (Bertin & Arnouts 1996). For the remaining bands, aperture fluxes were extracted. Regions surrounding very extended galaxies and saturated stars were excluded. The final sample area is 9.1 deg². The geometry of the Boötes field is shown in Fig. 6.1.

6.3.2 Additional Multiwavelength Surveys

The Boötes field has been surveyed in the X-ray band: XBoötes is a 5 ks survey which was performed with ACIS-I on the *Chandra* X-Ray Observatory (Murray et al. 2005). This is a large (9.3 square degree) contiguous region imaged in the X-ray that has complementary deep optical and NIR observations. The source catalogue (Kenter et al. 2005) contains 3,293 sources down to a 4 count flux limit, corresponding to $4.7 \times 10^{-15} \text{ erg s}^{-1} \text{ cm}^{-2}$ in the soft band (0.5–2.0 keV), $1.5 \times 10^{-15} \text{ erg s}^{-1} \text{ cm}^{-2}$ in the hard band (2.0–7.0 keV), and $7.8 \times 10^{-15} \text{ erg s}^{-1} \text{ cm}^{-2}$ full X-ray band (0.5–7.0 keV). Brand et al. (2006) provide a catalogue of 3,213 sources matched to the NDWFS DR3 catalogues using a Bayesian identification scheme.

Boötes is part of the *Herschel*² Multi-tiered Extragalactic Survey (HerMES; Oliver et al. 2012),

¹http://archive.noao.edu/nsa/NEWFIRM_NDWFS.html

²Herschel is an ESA space observatory with science instruments provided by European-led Principal Investigator consortia and with important participation from NASA.

6 Radio AGN in the Boötes field:

which includes photometry using the Spectral and Photometric Imaging Receiver (SPIRE; Griffin et al. 2010) instrument at $250\mu\text{m}$, $350\mu\text{m}$, and $500\mu\text{m}$. Within HerMES, Boötes has level 5 coverage of $3.25 \deg^2$ to 5σ noise levels of 13.8, 11.3, and 16.4 mJy and level 6 coverage of $10.57 \deg^2$ to 5σ noise levels of 25.8, 21.2, and 30.8 mJy. In this paper, we use the third data release (DR3) cross-identification catalogues based on *Spitzer* MIPS $24\mu\text{m}$ source positions (Roseboom et al. 2010).

6.3.3 The AGN and Galaxy Evolution Survey

The AGN and Galaxy Evolution Survey (AGES; Kochanek et al. 2012) has provided redshifts for 23 745 galaxies and AGN across $7.7 \deg^2$ of the Boötes field. The survey used the Hectospec instrument (Fabricant et al. 2005) on the MMT to obtain $3700\text{--}9200\text{\AA}$ spectroscopy at a spectral resolution of 6\AA ($R \approx 1000$), and achieved a spectroscopic completeness of approximately 90 per cent (Kochanek et al. 2012; Cool et al. 2012). The median redshift of the galaxies in the survey is $< z > = 0.3$, spanning the range $0 \lesssim z \lesssim 0.8$. However, the spectroscopic redshift completeness for the matched LOFAR sources at $z > 1$ is less than 50 per cent. For this reason we derive photometric redshifts, described in the following section. AGES also provides photometric redshifts, calculated using the LRT code by Assef et al. (2010) that fits a combination of an early-type, late-type, star forming, and (obscured) AGNs to the observed broadband SEDs. The photometry they used is a subset of that used in this work.

6.4 SED fitting

For the sample of 889,007 optical sources in the Brown et al. (2007) psf-matched photometry catalogue with $m_I \leq 24$ mag, we perform spectral energy distribution (SED) fitting to determine photometric redshifts and galaxy parameters, including stellar mass, star formation rates and colours.

6.4.1 Photometric Redshifts

Photometric redshifts (z_{phot}) are calculated for all galaxies using the EAZY software (Brammer et al. 2008). EAZY determines the z_{phot} for galaxies by fitting their SEDs to linear combinations of templates. We use an empirical set of templates derived from the atlas of 129 spectral energy distributions for nearby galaxies presented by Brown et al. (2014), with wavelength coverage spanning from the ultraviolet to the mid-infrared. This atlas spans a broad range of galaxy types, including ellipticals, spirals, merging galaxies, blue compact dwarfs, and luminous infrared galaxies. We select the subset of the Brown et al. (2014) templates given in their Appendix A. We found that this template set gave improved fits when including the MIR data points. A detailed description of EAZY's fitting process can be found in Brammer et al. (2008). Photometric redshifts were determined with EAZY primarily using the default set of parameters, using the Brown et al. (2014) templates, the K_s total magnitude prior, and allowed photometric redshift solutions in the range $0 < z < 6$.

The output EAZY photometric redshift catalogue contains the following columns:

Column 1 – id: Object identifier number

Column 2 – z_spec: Spectroscopic redshift, z_{spec} , from AGES (−1 indicates no redshift available)

Table 6.1: Sample photometric redshift catalogue.

id	z_{spec}	χ^2	z_{peak}	l68	u68	195	u95	199	u99	P_{peak}	N_{filt}
419194	-	3.4	1.569	1.099	2.092	0.699	2.545	0.207	2.853	0.998	12
420412	0.201	2.8	0.397	0.338	0.454	0.288	0.506	0.243	0.553	1.000	12
421383	-	6.0	0.427	0.285	0.578	0.172	0.673	0.084	0.768	1.000	13
421917	0.129	6.8	0.155	0.105	0.205	0.068	0.259	0.039	0.324	1.000	14
422118	0.778	29.2	0.779	0.687	0.870	0.596	0.933	0.515	0.996	0.999	14
424293	0.265	5.1	0.335	0.259	0.412	0.209	0.472	0.168	0.534	1.000	12
424369	-1.887	9.2	0.865	0.811	0.920	0.765	0.971	0.719	1.022	0.999	14
424393	-	9.6	1.506	1.363	1.659	1.272	1.805	1.188	1.988	0.999	13
424564	-	5.3	1.926	1.656	2.208	1.452	2.539	1.286	2.956	0.998	13
425016	0.267	1.2	0.352	0.287	0.416	0.239	0.471	0.198	0.516	1.000	12
425169	-	38.6	1.745	1.625	1.854	1.551	2.000	1.485	2.166	0.999	14
425332	0.126	26.6	0.470	0.306	0.609	0.224	0.680	0.168	0.751	0.999	14
426478	-	36.4	1.370	1.254	1.479	1.136	1.596	1.029	1.697	0.999	13
427404	0.212	15.2	0.374	0.298	0.443	0.223	0.547	0.170	0.646	1.000	14
427488	0.134	28.7	0.122	0.089	0.154	0.059	0.179	0.030	0.210	1.000	14

Column 3 – chi2: χ^2 of the best-fitting template

Column 4 – z_{peak} : Photometric redshift, z_{peak} , from the peak of the $P(z)$ distribution

Columns 5 and 6 – l68, u68: Upper and lower 68 per cent confidence intervals on z_{peak}

Columns 7 and 8 – 195, u95: Upper and lower 95 per cent confidence intervals on z_{peak}

Columns 9 and 10 – 199, u99: Upper and lower 99 per cent confidence intervals on z_{peak}

Column 11 – p_{z} : Peak probability, P_{peak}

Column 12 – n filt: Number of filters, N_{filt} , used to determine z_{peak}

The parameter z_{peak} corresponds to the peak probability of the $P(z)$ function, and is considered to be the most likely z_{phot} . The 68 per cent and 95 per cent confidence intervals are calculated by integrating the $P(z)$ function. A sample of the photometric redshift catalogue is shown in Table 6.1.

Comparison with AGES Redshifts

In Fig. 6.2 we show a comparison between the EAZY z_{phot} and z_{spec} for the sources with good AGES spectroscopic redshifts (with a signal-to-noise > 5). In general, the photometric redshifts compare well to the spectroscopic redshifts, although we note that this comparison is primarily from galaxies at $z_{\text{spec}} < 1.0$. Galaxies that are $> 3\sigma$ outliers from the one-to-one relation based on their redshift errors from EAZY are catastrophic outliers, the fraction of which is 1.8 per cent. As a measure of the accuracy of the photometric redshifts, we consider two quantities, computed after excluding the catastrophic outliers. The first goodness measure is the standard dispersion,

6 Radio AGN in the Boötes field:

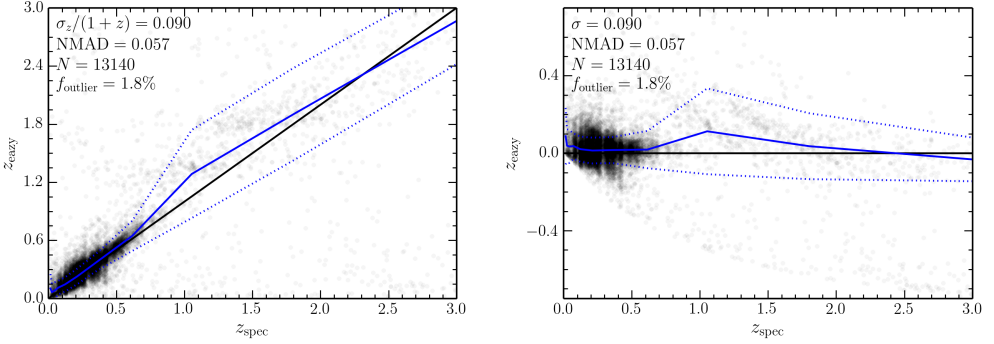


Figure 6.2: *Top panel* Photometric redshifts from the Boötes I -selected catalogue vs. spectroscopic redshifts from the AGES catalogue. Only galaxies with high-quality spectroscopic redshifts and uncontaminated photometry are shown. *Bottom panel* Difference between spectroscopic redshift and photometric redshift as a function of spectroscopic redshift. The solid and dotted blue curves show respectively the median and rms dispersion of $\delta z = (z_{\text{phot}} - z_{\text{spec}})/(1+z_{\text{spec}})$, within 11 logarithmic-spaced bins across the spectroscopic redshift range.

$\sigma_z/(1+z)$, defined by

$$\left(\frac{\sigma_z}{1+z} \right)^2 = \frac{1}{N} \sum_{i=1}^N \left(\frac{z_{\text{phot}}^i - z_{\text{spec}}^i}{1+z_{\text{spec}}^i} \right)^2. \quad (6.1)$$

The second is the normalized median absolute deviation, or NMAD, of the residuals, defined as $\text{NMAD}(\Delta z) = 1.48 \times \text{Median}(\Delta z)$, where $\Delta z = (z_{\text{phot}} - z_{\text{spec}})/(1+z_{\text{spec}})$. We measure $\sigma_z/(1+z) = 0.09$ and NMAD = 0.057. It is well known that photometric redshifts are poorly determined for AGN (Brodwin et al. 2006; Rowan-Robinson et al. 2008; Assef et al. 2010, e.g.), and should preferably be fit using different methods (e.g. Salvato et al. 2009, 2011). We compare the z_{phot} and z_{spec} for normal galaxies and AGN separately in Fig. 6.3. For this we use the sources flagged as AGN by Assef et al. (2010), which is based on their having a significant contribution by an AGN SED template. Excluding the galaxies selected as AGN in AGES, we find that the photometric redshifts are more accurate for normal galaxies, with $\sigma_z/(1+z) = 0.079$ and NMAD = 0.039. Considering only the AGES AGN, we find $\sigma_z/(1+z) = 0.24$ and NMAD = 0.12.

Assef et al. (2010) determine their redshifts to be more accurate, with $\sigma z/(1+z) = 0.04$ for normal galaxies $\sigma z/(1+z) = 0.18$ for point-like AGN. Although the photometric redshifts calculated here are not as good as those available from AGES, the sample is larger and complete, and the additional SED-fitting provides additional galaxy parameters (described in the next section). For comparison, the most accurate photometric redshift available typically have $\sigma z/(1+z) \lesssim 0.01$ (e.g. Ilbert et al. 2009; Muzzin et al. 2013), but using 30 bands of broad, intermediate and narrow width, and typically do not fit the longer wavelength MIR bands.

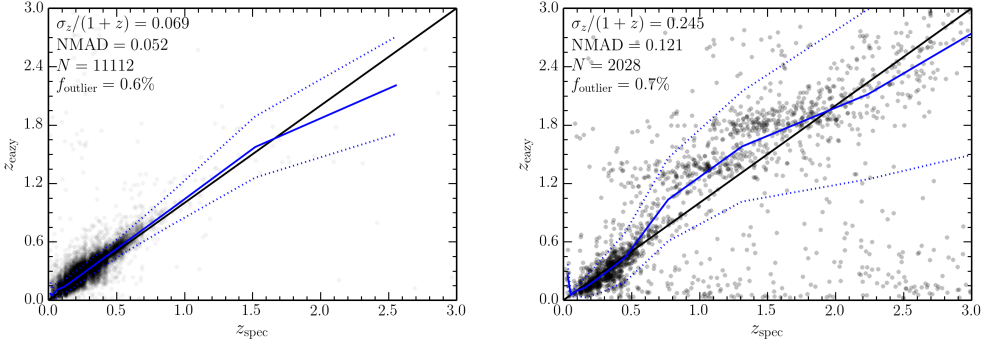


Figure 6.3: Photometric redshifts from the Boötes I -selected catalogue vs. spectroscopic redshifts from the AGES catalogue. *Left panel* Only galaxies not indicated as AGN in the AGES catalogue are plotted. *Right panel* Sources indicated to be AGN by the AGES SED fitting. The solid and dotted blue curves show respectively the median and rms dispersion of $\delta z = (z_{\text{phot}} - z_{\text{spec}})/(1 + z_{\text{spec}})$, within 11 logarithmic-spaced bins across the spectroscopic redshift range.

6.4.2 Stellar Masses, Star Formation Rates and Rest-frame Colours

Stellar population parameters are determined by fitting galaxy SEDs using the FAST code (Kriek et al. 2009), using the Bruzual & Charlot (2003) models. We assume solar metallicity, a Chabrier (2003) initial mass function (IMF), and a Calzetti et al. (2000) dust extinction law. The template SEDs are constructed in the standard way (see e.g. Muzzin et al. 2013), assuming exponentially declining star formation histories (SFHs) of the form $\text{SFR} \propto \exp(-t/\tau)$, where t is the time since the onset of star formation and τ is the e -folding star formation timescale in units of Gyr. All galaxies are fit assuming their redshift is the best-fit EAZY z_{phot} . In all, four parameters are determined per galaxy: τ , t , A_V , and a normalization. The stellar mass (M_*) is then determined from mass-to-light ratio of the best-fit SED multiplied by the best-fit normalization of the SED. The layout of the catalogue of stellar population parameters is:

Column 1 – id: Object identifier number

Column 2 – z: Photometric redshift, z_{peak} from EAZY

Column 3 – ltau: Best-fit value of $\log(\tau)$

Column 4 – lage: Best-fit value of $\log(t)$

Column 5 – Av: Best-fit value of A_V

Column 6 – lmass: Best-fit value of $\log(M_*/M)$

Column 7 – lsfr: Best-fit value of $\log(sfr)$ from the SED

Column 8 – lssfr: Best-fit value of $\log(ssfr)$ from the SED

Column 9 – chi2: χ^2 of best-fitting model

A sample of the FAST catalogue is shown in Table 6.2. We compare the stellar masses derived by FAST with a stellar mass calculated from the rest-frame colour, $g - i$, and absolute magnitude, M_i , (Taylor et al. 2011). This is shown in Fig. 6.4. There is good agreement between the two values across three orders of magnitude in mass.

Rest-frame colours are derived using INTERREST (Taylor et al. 2009) with the EAZY photometric redshifts. We determine colours for the $^{0.1}u$ and $^{0.1}r$ bands, defined as the AB magnitudes

6 Radio AGN in the Boötes field:

Table 6.2: Sample FAST catalogue.

id	z_{peak}	$\log(\tau)$	$\log(t)$	A_V	$\log(M_*/M)$	$\log(sfr)$	$\log(ssfr)$	χ^2
419194	1.56	10	9.4	0.8	10.08	0.84	-9.24	0.523
420412	0.21	8.5	9.0	2.0	10.62	0.97	-9.65	1.670
421383	0.41	7	7.8	1.2	8.82	-0.79	-9.61	0.754
421917	0.11	7.5	7.0	2.6	9.05	2.00	-7.04	3.370
422118	0.76	9	9.2	1.2	10.57	1.19	-9.38	4.340
424293	0.26	10	9.0	2.0	10.46	1.62	-8.84	2.700
424369	0.86	8.5	9.2	1.0	11.02	0.57	-10.44	1.230
424393	1.51	9.5	9.0	1.8	11.18	2.29	-8.89	1.500
424564	1.91	10	8.6	2.2	10.9	2.44	-8.46	0.327
425016	0.26	7	8.4	1.8	10.3	-7.13	-17.43	2.540
425169	1.76	7	7.4	1.0	10.07	2.09	-7.98	3.850
425332	0.11	7.5	7.4	3.0	8.77	1.25	-7.52	4.490
426478	1.36	9.5	9.0	1.8	10.97	2.09	-8.89	5.250
427404	0.21	10	8.8	2.2	10	1.35	-8.65	4.280
427488	0.11	7	7.0	3.0	8.72	1.51	-7.20	4.640

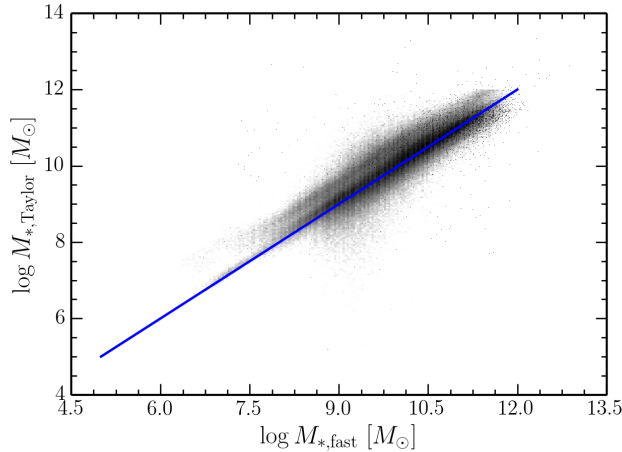


Figure 6.4: Comparison between stellar mass determined from FAST and rest-frame colour, $g-i$, and absolute magnitude, M_i . The greyscale shows log density.

in the SDSS u and r bands at $z = 0.1$. These colours allow straightforward comparison to SDSS results (e.g. Blanton et al. 2003c,b; Kauffmann et al. 2003; Blanton et al. 2003a).

6.5 Optical identification of Radio Sources

In this section we describe the identification of optical counterparts, from the I -band-selected optical catalogue described in Section 6.3, matched to the LOFAR radio sources, described in Section 6.2. We use the likelihood ratio (LR) method (Richter 1975) to quantify the probability of an I -band optical source being the true host of a given radio source. The LR method has been further developed by Prestage & Peacock (1983); Benn (1983); Wolstencroft et al. (1986) and Sutherland & Saunders (1992). Here we use the methodology outlined by Tasse et al. (2008a). Prior to the LR estimate, we inspect the images of each of the radio sources overlaid upon the corresponding I -band images, and classify their radio morphologies into different classes.

6.5.1 Visual Classification

In order to identify the host galaxies of radio sources, the true location of the host galaxy with respect to radio source should be known. Following Best et al. (2003) and Tasse et al. (2008a) we determine a strong subjective a priori of this location for each source by visually inspecting all the radio-optical images and dividing them into the following classes based on the radio morphology: *Class 1*: for these sources the radio emission is assumed to be coincident with the optical emission (detected or not). This occurs in sources such as starburst galaxies, compact core dominated radio sources or radio sources where the radio core can be clearly identified. In these cases, the errors on the radio and optical positions can be used in a statistical way to identify the optical counterpart of each radio source. We note that because of some bandwidth- and time-smearing in the LOFAR image (see Williams et al. 2015, submitted), we consider some radio sources which appear resolved to be unresolved point sources.

Class 2: in the case that no radio core is identified (such as for classical double lobe FRII (Fanaroff & Riley 1974) radio sources, only a weak a priori can be considered for the optical host position. The position of the host and associated errors are estimated based on the location of the multiple Gaussian fitting components, described in more detail in Best et al. (2003)

Class 3: when the environment has a large effect on the radio morphology, the flux weighted radio centroid and associated errors can be very far from the real optical host. We use the combination of radio morphology and optical properties (such as an elongated lobe pointing to a bright optical object), to infer the position of the optical counterpart.

Class 4: these are clearly resolved and diffuse radio sources whose morphology is not suggestive of jets. This includes radio halos and relics. These sources are excluded from further analysis.

Class 5: when the radio source overlaps a bright saturated source, we have classified the source as Class 5. These sources likely have contaminated photometry and are excluded in further analysis.

6.5.2 Likelihood Ratio

The probability that an optical I -band source is the true optical counterpart of a given radio source is determined from the likelihood ratio (LR; Sutherland & Saunders 1992; Tasse et al. 2008a),

6 Radio AGN in the Boötes field:

defined as:

$$LR(r, m) = \frac{\theta(< m) \exp\left(-\frac{r^2}{2}\right)}{2\pi\sigma_\alpha\sigma_\delta\rho(< m)}, \quad (6.2)$$

where m is the I -band magnitude of the optical candidate, $\theta(< m)$ is the a priori probability that a radio source has an observed optical counterpart with magnitude $< m$, and $\rho(< m)$ is the surface number density of objects with magnitude $< m$. The parameter r is the uncertainty-normalised angular distance between the radio core and the optical host candidate, defined as $r^2 = (\Delta\alpha/\sigma_\alpha)^2 + (\Delta\delta/\sigma_\delta)^2$, where Δ is the positional difference, σ is the uncertainty, and α and δ are the right ascension and declination respectively. For each α and δ , the uncertainty is the quadratic sum of the uncertainty on the radio position, σ_{radio} , and on the optical position, σ_{opt} . We adopt an optical astrometry accuracy of $\sigma_{\text{opt}} \sim 0.5$, independent of the magnitude m_I . The accuracy of the radio position, σ_{radio} , is different for every source and depends on the local noise level in the radio data and the Gaussian fitting parameters (Williams et al. 2015, submitted). The probability $P_{id}(i)$ of the i -th candidate being a true identification is:

$$P_{id}(i) = \frac{LR_i(r, m)}{\sum_j LR_j(r, m) + [1 - \theta(m_{\text{lim}})]}, \quad (6.3)$$

where $\theta(m_{\text{lim}})$ is the fraction of radio sources having detected optical counterparts at the limiting magnitude of the survey, i refers to the candidate under consideration and j runs over the set of all possible candidates. We estimate the association probability assuming that θ and ρ depend only on the object magnitude m , which is taken as the I -band magnitude of the optical candidate. For each radio source we calculate the density function $\rho(m)$ within $2'$ of the radio source centroid, in order to account for the variation of the surface density with position, or clustering of optical sources. To estimate the function $\theta(< m)$, we follow the methodology of Tasse et al. (2008a). This involves simulating random radio and optical catalogues with a known fraction of radio-optical matches and comparing the simulated radio-optical separation distribution to the real distribution. We consider discrete I -band magnitude cuts in the interval $13 < i < 24$ with an increment $\Delta m_I = 0.2$. For each of these cuts a radio catalogue having uniformly distributed positions is generated, along with a set of optical catalogues. Each optical catalogues in the set is generated by assigning a given fraction, $\theta(< m)$, of radio sources an optical counterpart. The optical hosts of radio sources then have their positions scattered by the radio and optical positional uncertainties. The distribution of the angular distance between radio sources and their closest object in the optical catalogue is then computed and compared to the real distribution through a Kolmogorov-Smirnov test. The retained fraction, $\theta(< m)$, is the one corresponding to the maximum Kolmogorov-Smirnov probability. For each I -band magnitude cut, the test is repeated 10 times, to estimate an error on $\theta(< m)$. Fig. 6.5 shows the variation of $\theta(< m)$ with the limiting magnitude.

6.5.3 Match Results

Of the 5 652 sources in the LOFAR 150 MHz catalogue, 3 317 lie within the boundary of the optical catalogue and may therefore have potential optical-counterparts. Of these 3 317 sources, we found 2 555 sources with optical counterparts with $m_I < 24$ mag for 2 326 unique radio sources (70 per cent). The majority of these sources were classified as Class 1 (3,033, 92 per cent), 113 sources (3.4 per cent) were classified as Class 2, 33 sources (1 per cent) were classified as Class 3,

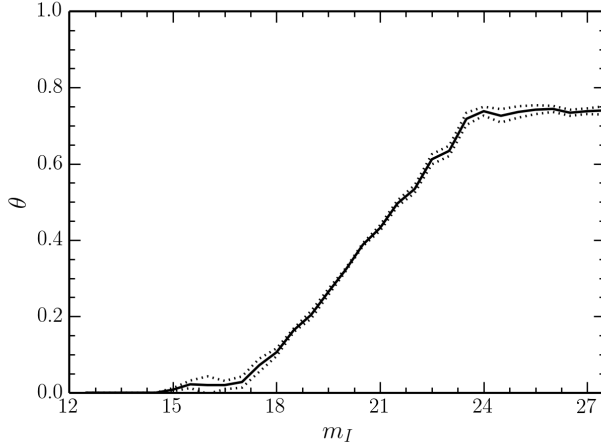


Figure 6.5: Fitted $\theta(< m)$, the a priori probability that a radio source has an observed optical counterpart with magnitude $< m$, as a function of the limiting magnitude. This is determined by simulating random radio and optical catalogues with a known fraction of radio sources and comparing to the observed distribution.

and 24 sources (1 per cent) were classified as Class 4. The remaining sources are Class 5 sources, with bad optical photometry. Some examples of the Class 1 and 2 sources with LR-matched optical sources are shown in Fig. 6.A.1 and Fig. 6.A.2 respectively in Appendix 6.A.

Fig. 6.6 shows the redshift distribution of all the matched radio-optical sources. A small number (30) of sources lie have photometric redshifts in the range $3 < z < 6$. The dotted lines in this image show the distribution of sources with spectroscopic redshifts from AGES – the low completeness of which motivates the need for a complete sample with photometric redshifts. Throughout the rest of this paper we adopt the z_{spec} from AGES where possible, else we use the EAZY z_{phot} . The radio-power versus redshift for these sources is shown in Fig. 6.7.

6.5.4 Contamination

In order to estimate the level of contamination by random matches, we generated 15 radio catalogues by randomising the positions of the sources in the real radio catalogue. We then cross-matched these 15 random radio catalogues with the optical sources in the same manner as described in the previous section. The distribution of optical identifications in optical magnitude m_I and stellar mass are plotted in Fig. 6.8. The contamination is high for sources with low stellar masses. The total contamination is ≈ 15 per cent for sources with stellar masses $M_* < 10^{12} M_\odot$. However, for sources with stellar masses $M_* < 10^9 M_\odot$ the contamination exceeds 90 per cent. We therefore, do not consider stellar masses below this value in later analysis.

6 Radio AGN in the Boötes field:

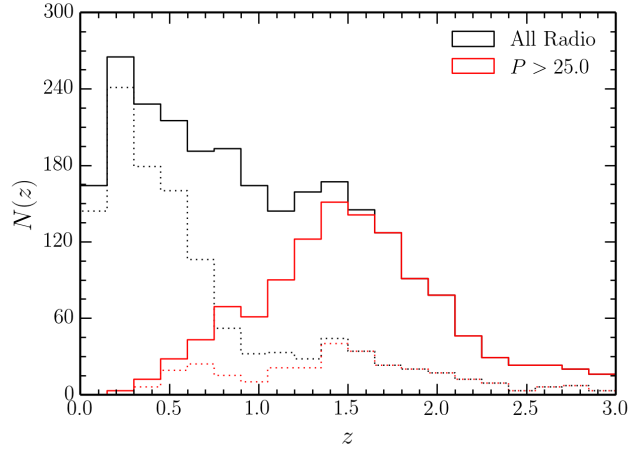


Figure 6.6: Redshift distribution. The high power sample defined in Section 6.6.2 is plotted in red and the full radio-optical sample is plotted in grey. The spectroscopic redshift distribution for each is plotted with dotted lines.

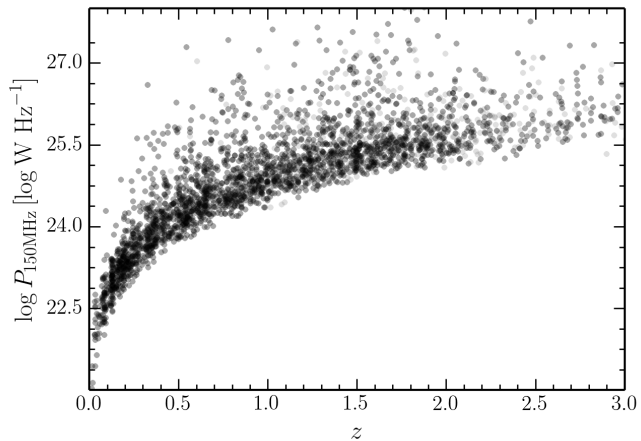


Figure 6.7: Distribution in the radio power vs. redshift plane of the matched radio-optical sources.

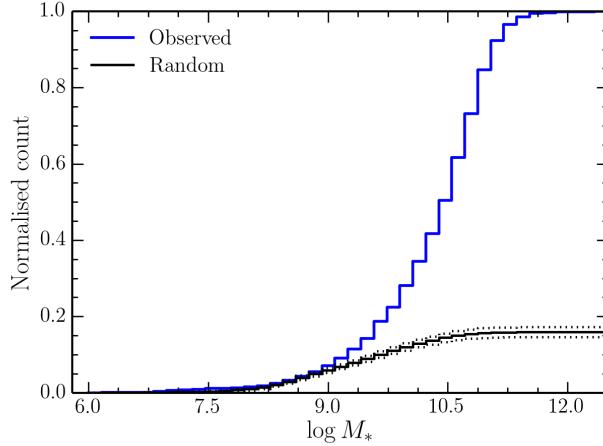


Figure 6.8: Stellar mass distributions for the observed sample (blue) and the 15 random radio catalogues (black). The total contamination is ≈ 15 per cent.

6.6 Properties of Radio Sources

6.6.1 Local Reference Sample

As a local comparison sample we use the catalogue compiled by Best & Heckman (2012). This matched radio-optical catalogue was constructed by from the seventh data release (DR7; Abazajian et al. 2009) of the Sloan Digital Sky Survey (SDSS) spectroscopic sample and the NRAO Very Large Array (VLA) Sky Survey (NVSS; Condon et al. 1998) and the Faint Images of the Radio Sky at Twenty centimetres (FIRST; Becker et al. 1995). The optical data includes parameters from the value-added spectroscopic catalogues (VASC) created by the Max Plank Institute for Astrophysics and Johns Hopkins University (MPA-JHU) group¹ (Brinchmann et al. 2004). This includes information from the imaging data such as magnitudes and sizes (York et al. 2000), as well as derived properties including the stellar mass (Kauffmann et al. 2003). The spectroscopy also provides D_{n4000} (Balogh et al. 1999), a measure of the galaxy colour. Best & Heckman (2012) separated the sources into star-forming galaxies and RL AGN (7302 sources), which are further sub-divided into HERGs, LERGs and star forming (SF) galaxies, based on their optical photometric and spectroscopic parameters. Noting the different observed radio frequency, we select sources with $P_{1.4\text{ GHz}} > 10^{24} \text{ W Hz}^{-1}$, corresponding to $P_{1.4\text{ GHz}} > 10^{25} \text{ W Hz}^{-1}$, assuming a spectral index of $\alpha = -0.8$. This local radio-optical sample consists of 3736 radio sources between $0.01 < z \leq 0.3$.

¹available at <http://www.mpa-garching.mpg.de/SDSS/>.

6 Radio AGN in the Boötes field:

6.6.2 Subsample Selection

The aim of this paper is to study the population of radio-loud AGN at intermediate redshifts. The radio power is plotted as a function of redshift in Fig. 6.7, for all the matched LOFAR-optical sources. At low redshifts, $z \lesssim 0.3$, the radio-optical sample is dominated by low luminosity radio sources and contains very few high power sources, while at higher redshifts we can only probe high power sources. For this reason we can not use this sample to directly compare high luminosity sources at both low and high redshift. The shallow wide LOFAR surveys will provide the areal coverage needed for such a comparison low redshift sample.

The rms in the radio map varies across the field of view (see Williams et al. 2015, submitted) between $100\text{--}250 \mu\text{Jy beam}^{-1}$, meaning that at a given redshift the lowest power sources can only be detected over a smaller area. We make a relatively low cut on radio flux of $S_{151 \text{ MHz}} \geq 0.5 \text{ mJy}$, and account for incompleteness resulting from the varying detection area later. From the $P - z$ plane it is clear that at $z = 2$ we can observe sources only with radio powers above $P_{1.4 \text{ GHz}} \geq 10^{25} \text{ W Hz}^{-1}$. In this paper we therefore study only the high power sources at intermediate redshifts $0.5 \leq z < 2$. The final sample consists of 974 sources, which we divide the sample in to three redshift intervals:

1. $0.5 \leq z < 1.0$ (173 sources),
2. $1.0 \leq z < 1.5$ (336 sources),
3. $1.5 \leq z < 2.0$ (273 sources).

Note that at radio powers $P_{1.4 \text{ GHz}} \gtrsim 10^{25} \text{ W Hz}^{-1}$ (corresponding to $P_{1.4 \text{ GHz}} \gtrsim 10^{24} \text{ W Hz}^{-1}$, for a spectral index of -0.8), the samples should consist almost entirely of radio-loud AGN – we expect very little contamination from star-forming galaxies. The star formation rate for this radio power is in excess of $25 M_{\odot} \text{ yr}^{-1}$ (Condon 1992).

6.6.3 IR SED fitting

While Gürkan et al. (2014) have suggested that a single cut in $22 \mu\text{m}$ flux can be used to separate LERGs and HERGs, our investigation using the complete lower luminosity sample from Best & Heckman (2012) indicates that this may be a result of selection effects (Rigby et al. 2015, in prep.). We therefore attempt to separate these sources based on further SED fitting to determine the AGN and galaxy contribution to their IR emission. For this fitting we have included the FIR fluxes of these sources at $250 \mu\text{m}$, $350 \mu\text{m}$, and $500 \mu\text{m}$ by matching to the HerMES catalogue for the Boötes Field (Oliver et al. 2012). The *Herschel* fluxes were found by matching the nearest neighbour to the optical positions within the *Herschel* beam sizes at each wavelengths. About 70 per cent of the sources have a detection in HerMES at either $250 \mu\text{m}$ or $350 \mu\text{m}$. The FIR fluxes provide an important constraint to separate the starformation and AGN components. In order to decompose the SEDs of the sources we fit all the available multiwavelength photometry, including FIR, using the MCMC-based algorithm AGNFITTER (Calistro Rivera et al. 2015, in prep.). We have done this for the sub-sample of 974 sources.

An advantage of using AGNFITTER is that it infers the probability density functions (PDFs) of the fitting parameters. This allows correlations and degeneracies among parameters to be recognised and allows for a robust calculation of the uncertainties for the inferred parameter values. The

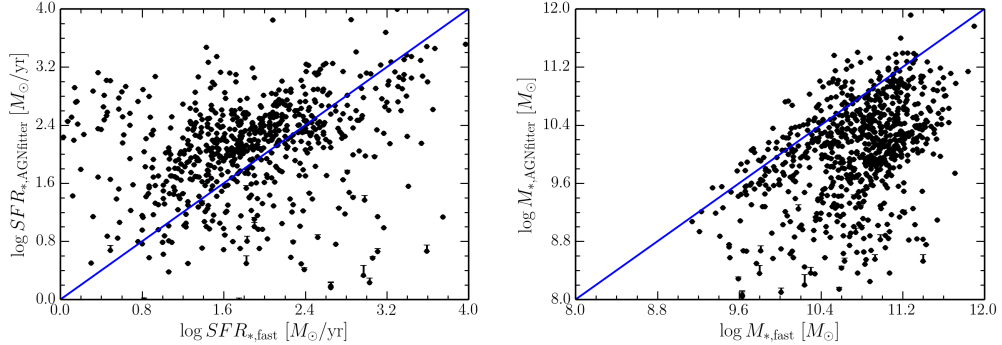


Figure 6.9: Comparison between SFR (left) and stellar mass (right) determined by FAST and AGNFITTER.

total active galaxy model in AGNFITTER consists of the superposition of the host galaxy emission and the nuclear AGN emission. The host galaxy is modelled as a combination of a stellar emission and the reprocessed emission of cold/warm dust in starburst (SB) regions. At nuclear scales, the AGN emission is modelled as a combination of an accretion disk component (Big Blue Bump) and a hot dust torus component.

The parameters of interest for our purposes are the disentangled host galaxy and AGN luminosities that contribute to the IR emission. While the AGN contribution, which affects specifically the MIR regime, arises mainly from the torus luminosity L_{TO} , the contribution from galaxy emission takes into account both the stellar emission L_{GA} and the reprocessed emission by cold/warm dust L_{SB} , since both have contributions in the MIR. For the matter of comparison, these luminosities are integrated over the respective templates in a single wavelength range $1\mu\text{m} < \lambda < 8\mu\text{m}$.

A small fraction of sources (183, ≈ 7 per cent) have very poor fits, i.e. have AGNFITTER likelihood values < -100 . These are excluded in further analysis. Some examples of the AGNFITTER SEDs with components in the three redshift intervals are shown in appendix 6.B in Fig. 6.B.1 and Fig. 6.B.2 for sources with good quality fits (quantified by likelihood values close to -1) and in Fig. 6.B.3 for sources with poor fits (quantified by likelihood values $\lesssim -20$).

As a test of the robustness of the AGNFITTER results, we compare the stellar masses and SFRs returned by AGNFITTER to those we have derived using FAST (see Section 6.4.2). This comparison is shown in Fig. 6.9.

HERG/LERG separation

We aim to differentiate between HERGs ('cold mode' or 'radiative mode' sources), and LERGs ('hot mode' or 'jet mode' sources) based on their broadband SED information. In the remainder of the paper we use the nomenclature of HERGs and LERGs for succinctness. From the AGNFITTER output we calculated the value,

$$f_{TO} = \frac{L_{TO}}{L_{TO} + L_{GA}}, \quad (6.4)$$

6 Radio AGN in the Boötes field:

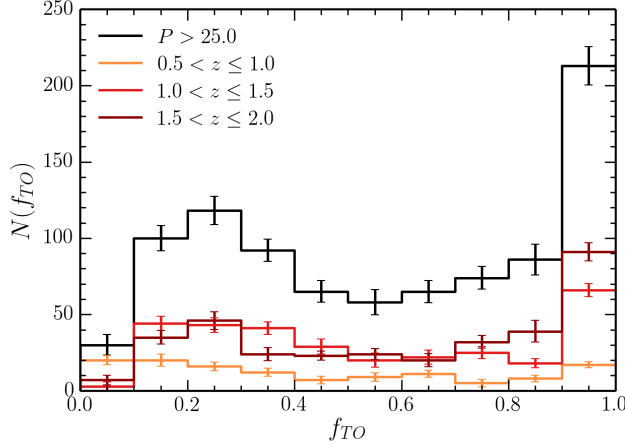


Figure 6.10: Distribution of the fraction of IR torus emission, f_{TO} , defined by equation 6.4 for the full sample (black), and the three redshift intervals: $0.5 \leq z < 1.0$ (orange), $1.0 \leq z < 1.5$ (red), and $1.5 \leq z < 2.0$ (dark red).

which is a measure of the fraction of IR-emission that is coming from the torus with respect to that from the galaxy, independent of the starburst component. The error of f_{TO} is calculated by propagating the errors on L_{TO} and L_{GA} given by AGNFITTER. The distribution of f_{TO} values is plotted in Fig. 6.10, where we show the distribution for all radio sources, and for within each of the three redshift intervals. We expect that HERGs have significant contribution to the IR emission from the torus, and that LERGs have little or no such contribution. There is a maximum in the overall distribution for sources with $0.9 < f_{TO} < 1$, and a minimum at $0 < f_{TO} < 0.1$, and we note that there is a difference in the distribution at $0.5 < z \leq 1.0$ compared to the two higher redshift intervals. The two highest redshift intervals both show the significant maximum at $f_{TO} \approx 1$ and minimum at $f_{TO} \approx 0$, which suggests that there are more ‘strongly AGN-dominated’ sources and fewer ‘AGN-free’ sources in these intervals than at $0.5 < z \leq 1.0$. Given the uncertainties in the SED fitting procedure, it is unclear where to place a boundary which would separate sources that contain IR AGN emission, i.e. HERGs, from those that contain completely no IR AGN, which would be LERGs. Theoretically, LERGs would have $f_{TO} \approx 0$, however, they may appear with non-zero values due to errors in the photometry and fitting. We therefore choose a conservative boundary value of $f_{TO} = 0.25$ and classify sources with $f_{TO} < 0.25$ as LERGs and $f_{TO} > 0.25$ as HERGs. This uncertainty highlights the need to perform similar SED fitting for a sample with spectroscopic classification of HERGs and LERGs, in particular for this specific set of photometry. For this reason follow-up spectroscopy of these optically-identified LOFAR radio sources will be valuable.

The example AGNFITTER SEDs shown in Figs. 6.B.1, 6.B.2 and 6.B.3 include both HERGs and LERGs classified in this way in each redshift interval. The number of HERGs and LERGs in each redshift interval are given in Table 6.3, including those taken from the local reference sample, from which it can be seen that the fraction of HERGs increases between $0.5 \leq z < 1.0$

Table 6.3: Number of sources classified as HERGs and LERGs in the reference sample and the three redshift intervals.

z	N	LERGs (%)	HERGs (%)
0.01–0.3	3736	3066 (96%)	121 (4%)
0.5–1.0	173	52 (30%)	121 (69%)
1.0–1.5	384	72 (18%)	312 (81%)
1.5–2.0	390	67 (17%)	321 (82%)

and $1.0 \leq z < 1.5$. The percentage of HERGs and LERGs within each redshift interval is given with respect to the total number of radio sources in that interval.

6.6.4 Star Formation contribution

Similarly, we define the quantity

$$f_{SB} = \frac{L_{SB}}{L_{SB} + L_{GA}}, \quad (6.5)$$

as a measure of the fraction of IR-emission that is coming from star formation with respect to that from the galaxy, independent of the AGN torus emission. The error of f_{SB} is calculated by propagating the errors on L_{SB} and L_{GA} given by AGNFITTER. In Fig. 6.B.1 we show examples of sources with high f_{SB} values for HERGs and LERGs in the three redshift intervals, and in 6.B.2 we show examples of sources with low f_{SB} values. The distribution of f_{SB} values is plotted separately for HERGs and LERGs in Fig. 6.11, where we show the distribution for all radio sources, and for within each of the three redshift intervals. LERGs have a peak at $f_{SB} \approx 0$ in all redshift intervals, with a secondary peak at $f_{SB} \approx 1$ in the two higher redshift intervals. This is suggestive of a population of LERGs in star forming galaxies. HERGs, on the other hand, have a peak at $f_{SB} \approx 1$ with a secondary peak at $f_{SB} \approx 0$. The peak at $f_{SB} \approx 1$ is largely due to the two highest redshift intervals. It is interesting to note that some HERGs are found in galaxies with very little star formation.

6.6.5 Colour-mass distribution

Having classified the sources as HERGs and LERGs based on their AGN contribution in the MIR, we now study the distribution of the radio-loud AGN with respect to their optical host colours and masses. For the local reference sample we plot the colour, given by the spectroscopic D_n4000 value, against the stellar mass Fig. 6.12. In Figs. 6.13, 6.14, and 6.15 we show, for each redshift interval, a plot of the $^{0.1}(u - r)$ colour versus stellar mass for optical sources and radio sources. The f_{TO} values for the radio sources are shown in colour and the distributions of stellar mass and colour are shown for the optical sources, the radio sources and the HERGs and LERGs. In comparing the local and higher redshift samples, we note that the parameters used are different, for both the colour and mass, and the HERG/LERG separation. However, they provide a qualitative comparison, for the distribution of the radio and optical source populations in colour-mass space. In all redshift intervals it is clear that the distributions of optical and radio

6 Radio AGN in the Boötes field:

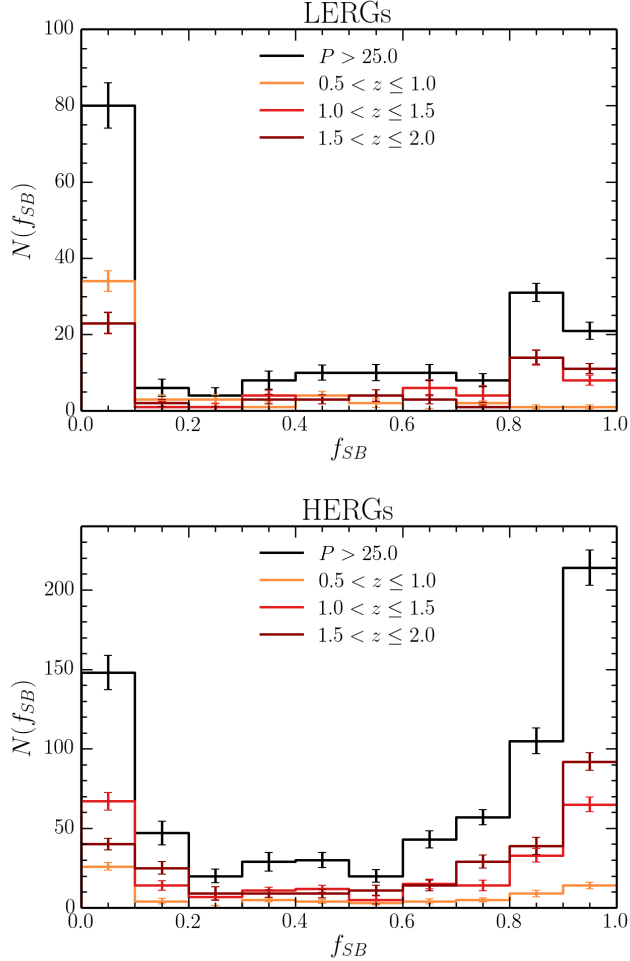


Figure 6.11: Distribution of the fraction of SB emission, f_{SB} , defined by equation 6.5, separately for LERGs (top) and HERGs (bottom), for the full sample (black), and the three redshift intervals: $0.5 \leq z < 1.0$ (orange), $1.0 \leq z < 1.5$ (red), and $1.5 \leq z \leq 2.0$ (dark red).

Table 6.4: Two-sided Kolmogorov-Smirnov statistics in comparing the HERG and LERG distributions in colour and mass within each redshift interval.

z	$0.1(u - r)$		$\log M_*/M_\odot$	
	K-S statistic	p -value	K-S statistic	p -value
0.5–1.0	0.56	$1.1 \cdot 10^{-10}$	0.52	$2.1 \cdot 10^{-9}$
1.0–1.5	0.24	$1.4 \cdot 10^{-3}$	0.29	$1.0 \cdot 10^{-4}$
1.5–2.0	0.38	$1.8 \cdot 10^{-7}$	0.39	$4.4 \cdot 10^{-8}$

sources are different, as expected. In all cases the radio source distribution is skewed towards more massive galaxies and redder galaxies compared to the full galaxy population. The distributions of HERGs and LERGs are also different, in that the HERGs occur over a wider range of stellar masses $10^9 < M_*/M_\odot < 10^{11.5}$ and over a wider range of colours. LERGs are much more likely to be in massive red galaxies. We use a two-sided Kolmogorov-Smirnov test, and in all cases can reject the null hypothesis that the distributions are the same. The Kolmogorov-Smirnov statistics and p -values are given in Table 6.4. We note that in these plots the radio source population is slightly incomplete due to the varying rms in the LOFAR map (see Section 6.6.2).

6.6.6 Radio-loud fraction

The mass-dependence of the radio-loud fraction can be an indicator of the accretion mode of the radio-AGN largely because of the different dependence of the fuelling source (hot vs. cold gas) on stellar mass (Best et al. 2006). As this is not a volume-limited sample, we use the radio-loud fraction defined by:

$$f_{\text{RL}}^{y,x} = \left(\sum_{i \in R^{y,x}} \frac{1}{V_{\max}^i} \right) \left(\sum_{j \in A^{y,x}} \frac{1}{V_{\max}^j} \right)^{-1}, \quad (6.6)$$

where the sets A and R are, respectively, all galaxies and all radio sources in a given bin, defined by the parameters of colour, x , and excitation state, y . V_{\max} is the maximum accessible volume over which each source can be observed, using the Schmidt (1968) and Condon (1989) formalism. This is determined by the flux limits of both the optical (< 24 mag) and radio data ($S_{151 \text{ MHz}} \geq 0.5 \text{ mJy}$). The maximum volume also takes into account the visibility area from the radio data, i.e. the area in which the radio source could be detected based on the varying rms map.

The radio-loud fraction for all radio sources, and separately for HERGs and LERGs is shown in Fig. 6.16. It can be seen that the radio-loud fraction for all sources at all masses increases with redshift. The dependence on stellar mass is flatter for HERGs than it is for LERGs at all redshifts. Table 6.5 gives the value of the slope fit to $\log f_{\text{RL}} - \log M_*/M_\odot$ over the range $10^9 < M_*/M_\odot < 10^{11.5}$. These results are consistent with those from many of the earlier radio surveys, which suggest that the most powerful radio galaxies ($P_{1.4 \text{ GHz}} \gtrsim 10^{26} \text{ W Hz}^{-1}$) at $z \gtrsim 1$ are predominantly HERGs hosted by the most massive galaxies (e.g. Eales et al. 1997; Jarvis et al. 2001; Seymour et al. 2007; Fernandes et al. 2015).

6 Radio AGN in the Boötes field:

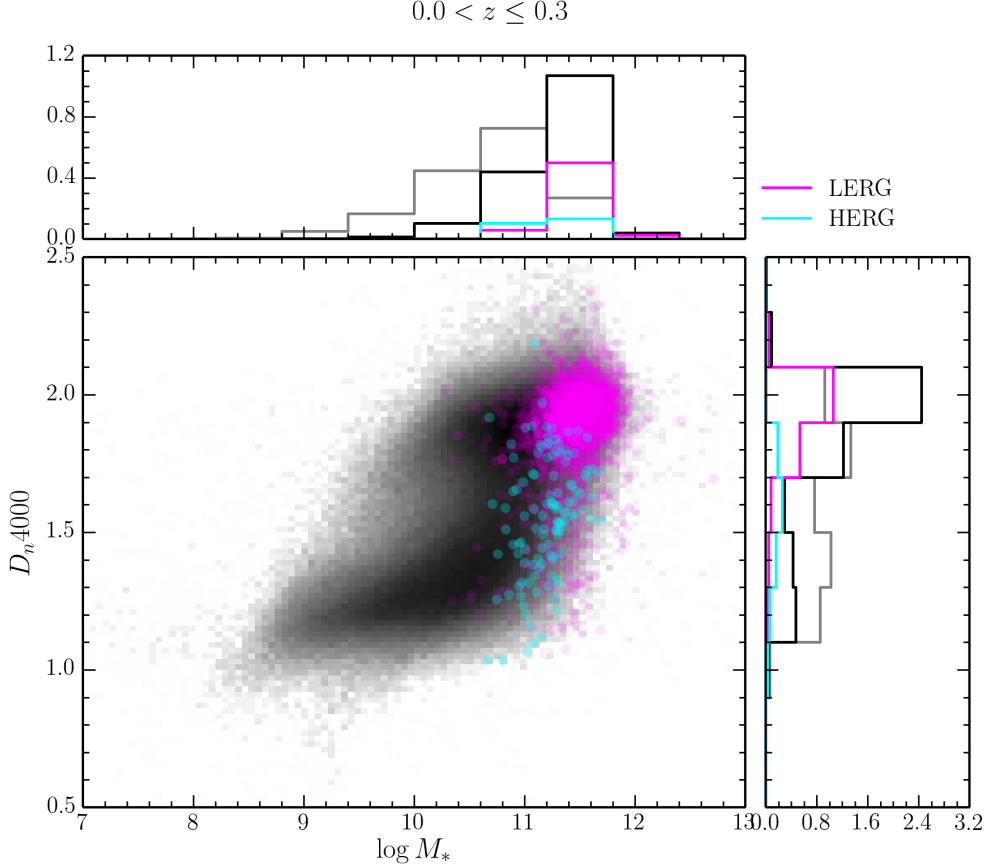


Figure 6.12: Colour, D_{n4000} , versus stellar mass in the redshift interval $0.01 \leq z < 0.3$ (main panel). The density of optical sources is plotted in black, in log units, and the radio sources are plotted in cyan (HERGs) and magenta (LERGs). The subpanels show the stellar mass (top) and colour distributions (right). The normalised distribution of optical sources is shown in grey, and that of all the radio sources in black. The HERGs and LERGs are shown in cyan and magenta respectively, normalised to the total number of radio sources. The HERG distributions is multiplied by a factor of 10 for visibility.

Table 6.5: Slope of the radio-loud fraction as a function of mass for HERGs and LERGs in the three redshift intervals.

z	All	LERGs	HERGs
0.5–1.0	1.25 ± 0.15	2.08 ± 0.28	0.93 ± 0.11
1.0–1.5	1.12 ± 0.10	1.70 ± 0.13	0.99 ± 0.09
1.5–2.0	1.05 ± 0.04	1.86 ± 0.21	0.93 ± 0.06

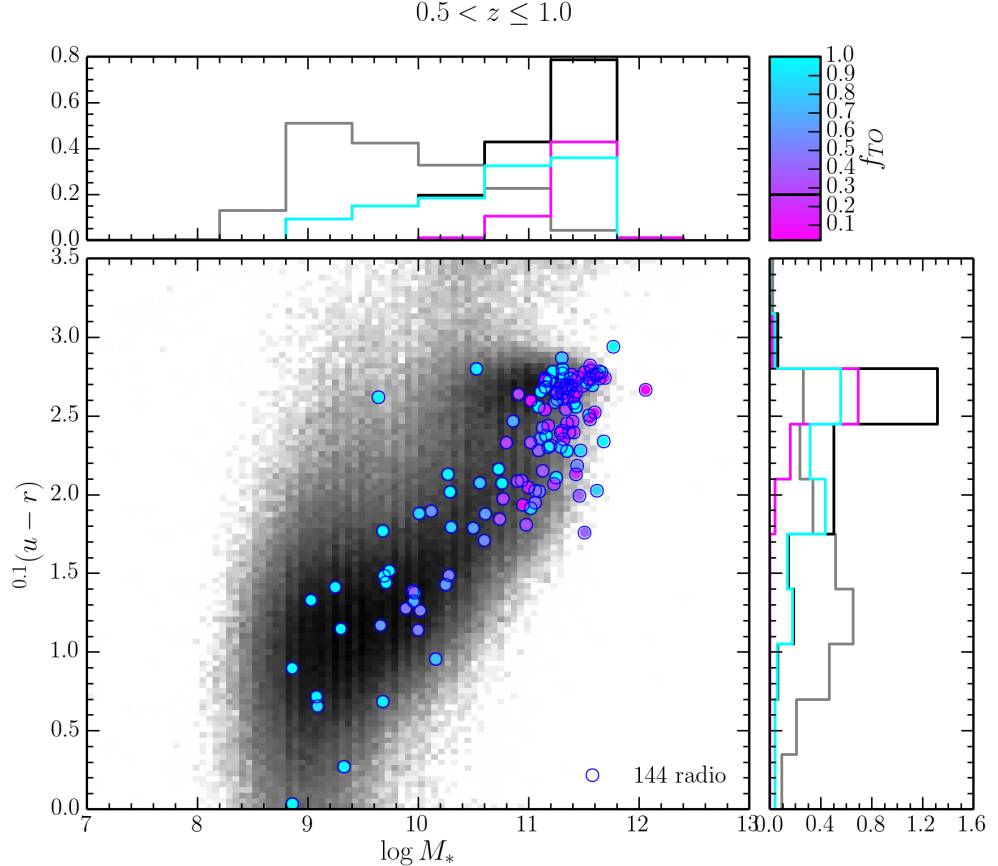


Figure 6.13: Colour, ${}^{0.1}(u - r)$, versus stellar mass in the redshift interval $0.5 \leq z < 1.0$ (*main panel*). The density of optical sources in the Boötes field is plotted in black, in log units, and the radio sources are plotted with blue circles, with the fill-colour indicating their f_{TO} values. Open circles show failed AGN FITTER fits. The subpanels show the stellar mass (*top*) and colour distributions (*right*). The normalised distribution of optical sources is shown in grey, and that of all the radio sources in black. The HERGs and LERGs (separated at $f_{TO} = 0.25$) are shown in cyan and magenta respectively, normalised to the total number of radio sources.

6 Radio AGN in the Boötes field:

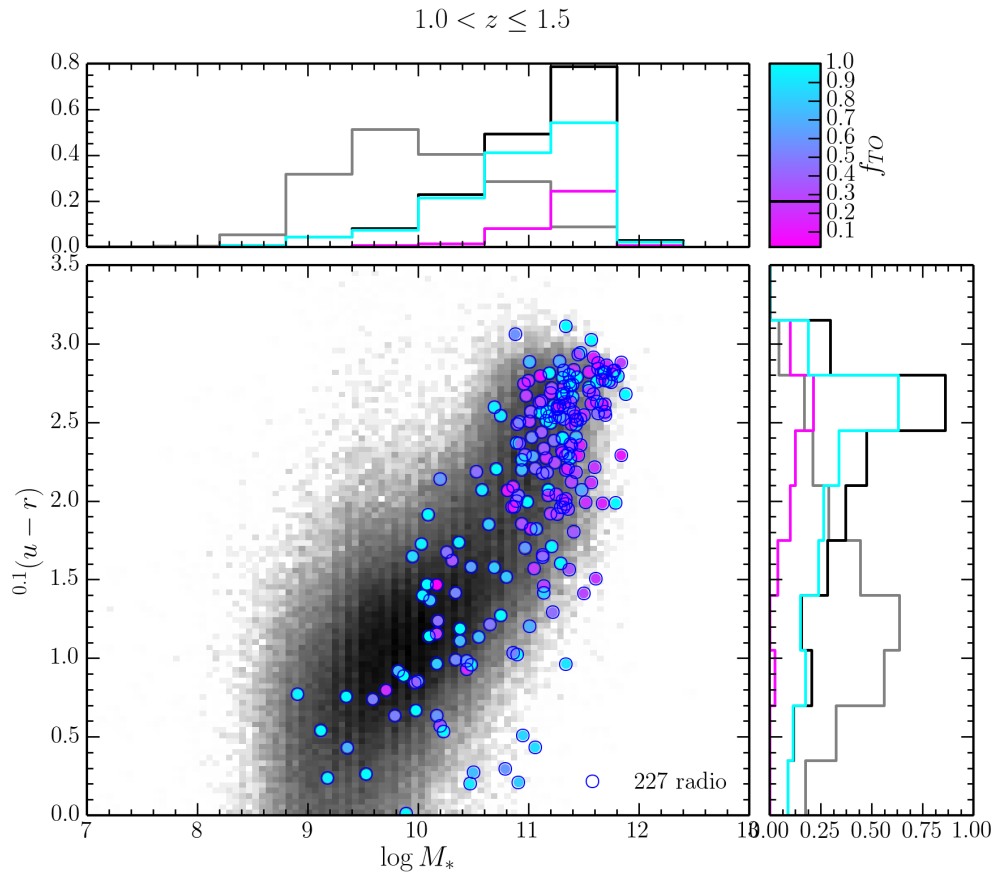


Figure 6.14: As for Fig. 6.13, but for the redshift interval $1.0 \leq z < 1.5$

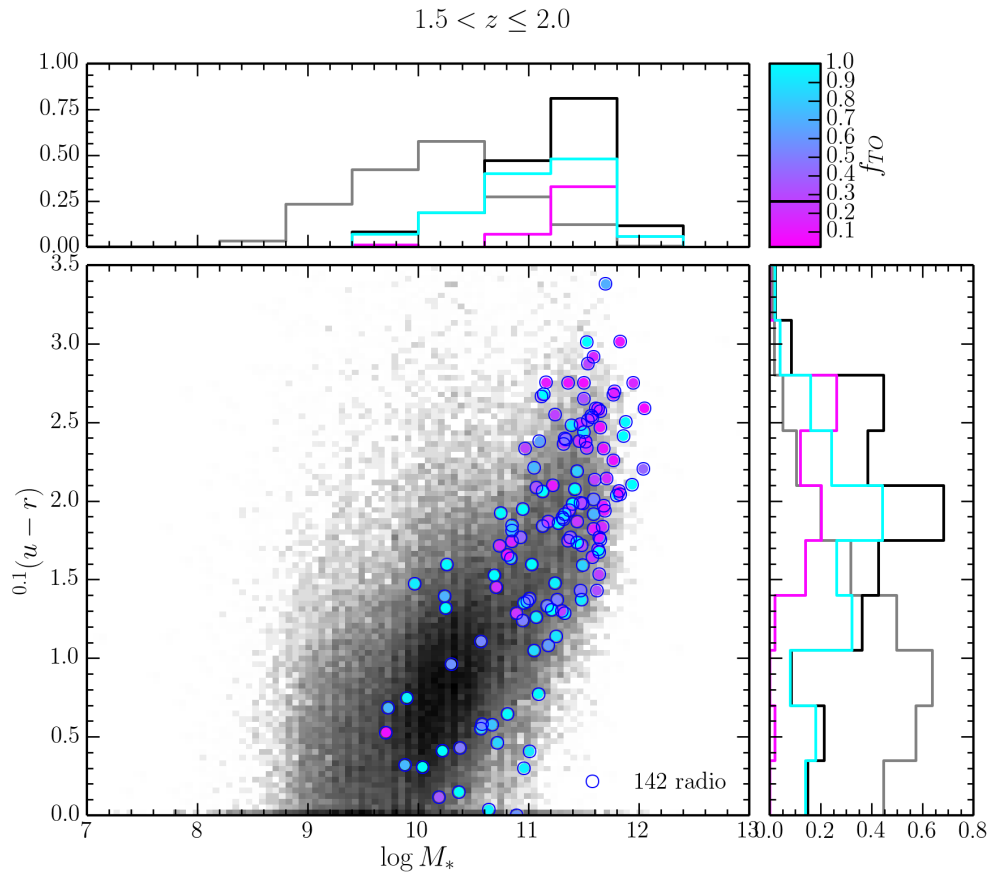


Figure 6.15: As for Fig. 6.13, but for the redshift interval $1.5 \leq z < 2.0$.

6 Radio AGN in the Boötes field:

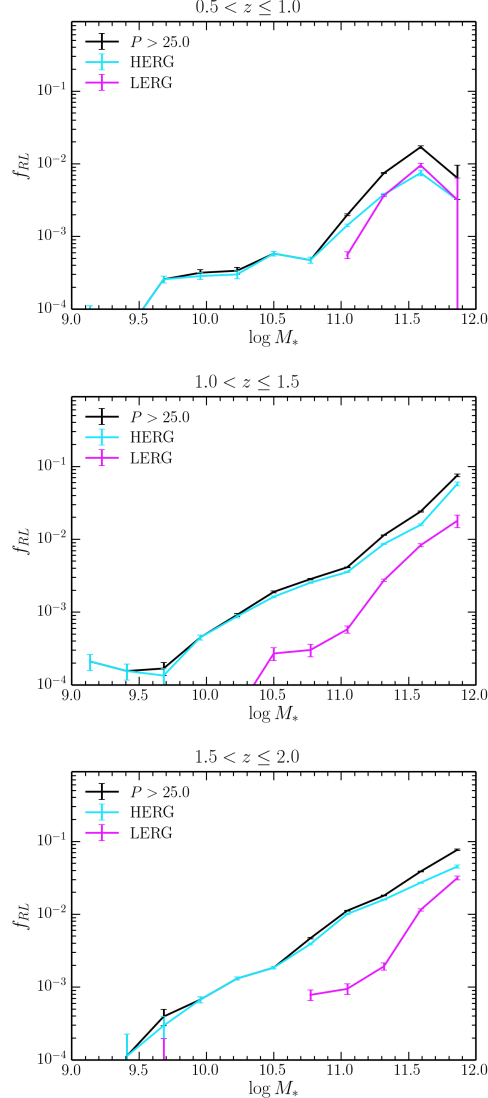


Figure 6.16: The fraction of galaxies hosting a radio source (radio-loud fraction) as a function of stellar mass for a radio-power cut-off of $P_{1.4\text{ GHz}} > 10^{25} \text{ W Hz}^{-1}$ in the three redshift bins. The errors are determined from Poisson statistics. All radio sources are plotted in black, HERGs in cyan and LERGs in magenta.

Table 6.6: Number of sources classified as blue and red HERGs and LERGs in the reference sample and the three redshift intervals.

z	N	BLERGs (%)	RLERGs (%)	BHERGs (%)	RHERGs (%)
0.01–0.3	3736	148 (3.9%)	2918 (78%)	61 (1.6%)	60 (1.6%)
0.5–1.0	173	17 (9%)	32 (18%)	89 (51%)	28 (16%)
1.0–1.5	384	52 (13%)	20 (5%)	248 (64%)	57 (14%)
1.5–2.0	390	55 (14%)	12 (3%)	301 (77%)	10 (2%)

In colour-magnitude space (not shown here), we use the empirically determined cuts to separate red and blue galaxies (Hickox et al. 2009) using the quantity:

$$A = {}^{0.1} (u - r) + 0.08 (M_{0.1r} + 20). \quad (6.7)$$

We use their median values of A for the red sequence of $A_{\text{red}} = 2.64$ in our first redshift interval and $A_{\text{red}} = 2.52$ in our second and third redshift intervals. The boundary between red and blue galaxies is set 0.3 mag blueward of the median values of A for the red sequence. The numbers of blue and red LERGs (BLERGs and RLERGs respectively) and HERGs (BHERGs and RHERGs respectively) within each redshift interval are listed in Table 6.6. This table also gives the fraction of each subgroup with respect to the number of radio-loud sources in each redshift interval. For the local reference sample, we use the $D_n 4000$ parameter to determine colour: sources with $D_n 4000 < 1.575$ are blue and sources with $D_n 4000 \geq 1.575$ are red.

We then calculate the radio-loud fraction separately for each subgroup. This is shown in Fig. 6.17. The fraction of BHERGs increases at all masses with redshift, while the fraction of RHERGs decreases. Janssen et al. (2012) have studied the radio-loud fraction for red, green and blue HERGs and LERGs in the local Universe ($0.03 \leq z \leq 0.3$). Since their colour-cut was made on the spectroscopic $D_n 4000$ value, we can only qualitatively compare our results to those in their Fig. 4 for red and blue galaxies for their power cut of $P_{1.4 \text{ GHz}} \geq 10^{24.5} \text{ W Hz}^{-1}$ (roughly equivalent to $P_{1.4 \text{ GHz}} \geq 10^{25.5} \text{ W Hz}^{-1}$).

6.7 Conclusion

We have constructed a catalogue of photometric redshifts, stellar masses, and rest-frame colours via SED fitting of the multi-band photometry catalogue (Brown et al. 2007) available for the Boötes field. We have identified optical counterparts from this catalogue of sources to radio sources from the 150 MHz LOFAR observations of the Boötes field (Williams et al. 2015, submitted). For a well-defined sub-sample of 974 radio sources with optical matches between $0.5 \leq z < 2$ and radio-powers above $P_{1.4 \text{ GHz}} > 10^{25} \text{ W Hz}^{-1}$, we have done additional SED fitting, including the FIR emission, to determine the relative contribution of AGN and galaxy emission in the MIR ($1 \mu\text{m} < \lambda < 8 \mu\text{m}$). From these results we have defined populations of HERGs and LERGs and studied the radio-loud fraction as a function of galaxy mass and colour. In summary, we have found the following:

1. The fraction of HERGs increases between $z = 0.5$ and $z = 2$;

6 Radio AGN in the Boötes field:

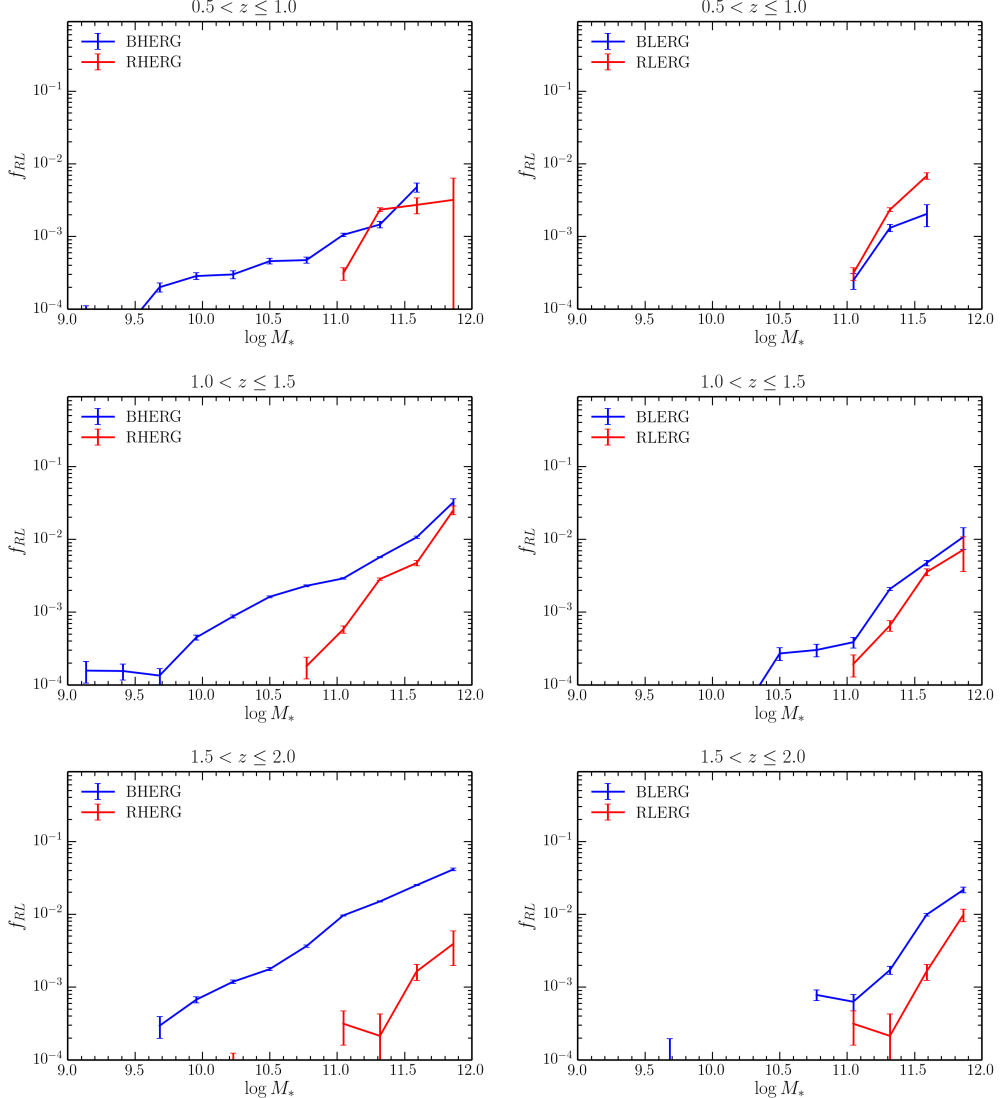


Figure 6.17: The fraction of red and blue galaxies hosting a radio source as a function of stellar mass for a radio-power cut-off of $P_{1.4} \text{ GHz} > 10^{25} \text{ W Hz}^{-1}$ in the three redshift bins (*top to bottom*) for HERGs (*left*) and LERGs (*right*). The errors are determined from Poisson statistics.

2. While most LERGs are found in dead galaxies, at $z > 1$ there is a population of LERGs in star forming galaxies; and HERGs are found in both star forming and dead galaxies;
3. LERGs are predominantly found in more massive galaxies than HERGs;
4. LERGs are predominantly found in redder galaxies, but at higher redshifts are bluer;
5. The radio-loud fraction for blue HERGs increases with redshift while that for red HERGs decreases with redshift for all masses

6.7.1 Future work

There remain a few open questions and issues relating to this work. These include the following:

1. The incorporation of the errors from AGN FITTER in the determination of f_{TO} will enable us to investigate how they affect the resulting radio-loud fractions.
2. It is important to understand how the AGN populations determined using the f_{TO} values from SED fitting, described in Section 6.6.3, relate to the spectroscopically-classified populations. This could be done by comparing the AGN FITTER output for spectroscopically classified sources. Initially this should involve using AGN FITTER to investigate how f_{TO} varies for existing spectroscopically-classified HERGs and LERGs. In the future, follow-up spectroscopy of this sample will shed light on the quality of the f_{TO} results for this dataset.
3. We have no comparison sample at low redshift with which to directly track the evolution from $z \approx 0$. This will be possible with the wide area surveys currently underway with LOFAR, combined with the SDSS-NVSS sample (Best & Heckman 2012)

Acknowledgements

WW, HJR gratefully acknowledge support from the European Research Council under the European Union's Seventh Framework Programme (FP/2007-2013) /ERC Advanced Grant NEW-CLUSTERS-321271. This research has made use of data from HerMES project¹. HerMES is a Herschel Key Programme utilising Guaranteed Time from the SPIRE instrument team, ESAC scientists and a mission scientist. The HerMES data was accessed through the Herschel Database in Marseille (HeDaM²) operated by CeSAM and hosted by the Laboratoire d'Astrophysique de Marseille.

Appendix

6.A Radio-Optical Matches

Some examples of the Class 1 and 2 sources with LR-matched optical sources are shown in Fig. 6.A.1 and Fig. 6.A.2 respectively.

¹<http://hermes.sussex.ac.uk/>

²<http://hedam.lam.fr>

6 Radio AGN in the Boötes field:

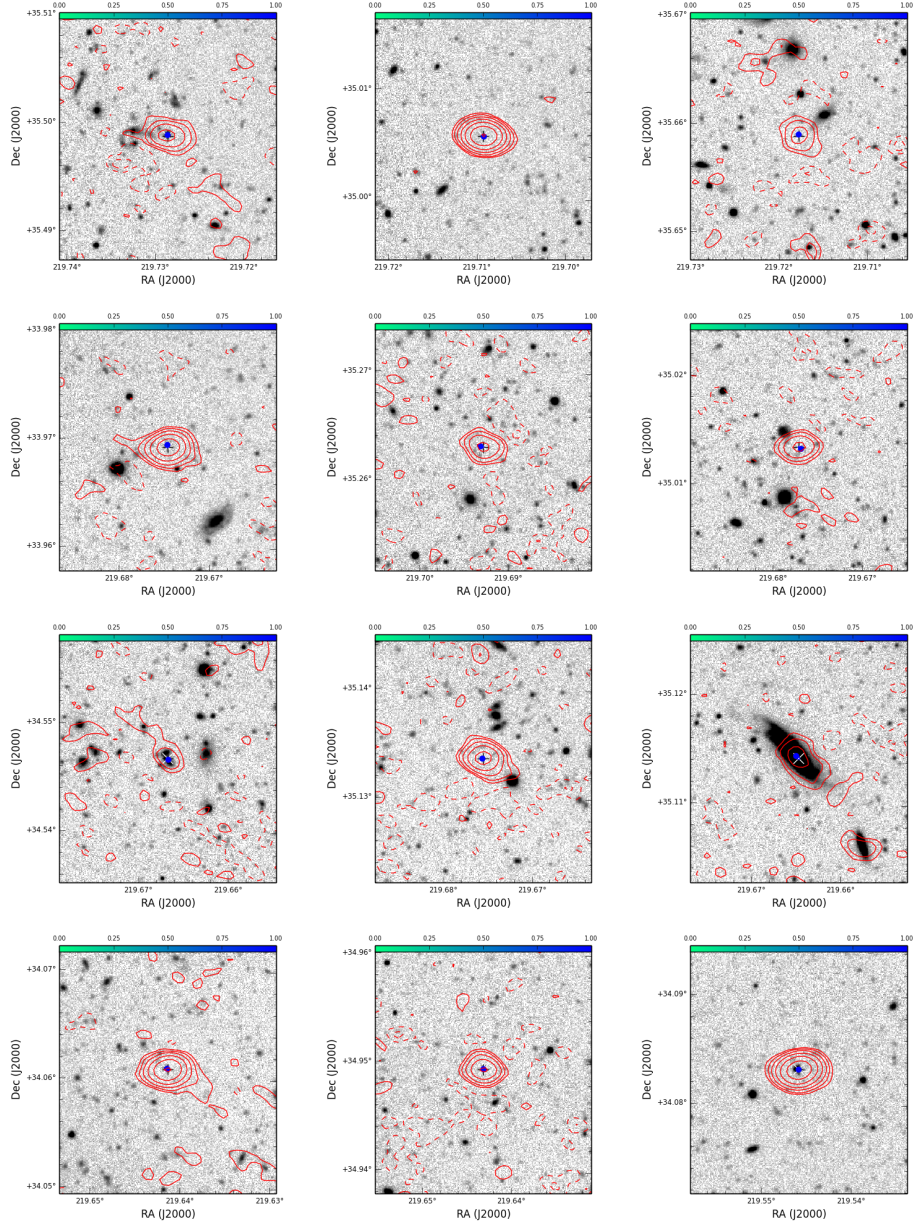


Figure 6.A.1: Examples of the radio-optical cross matches in Class 1. The greyscale image show the I -band NDWFS image. The red contours show the LOFAR 150 MHz image at levels of $3\sigma_{\text{local}} \times [1, 1.4, 2, 2.8, \dots]$ where σ_{local} is the local rms in the LOFAR map at the source position. The blue colorscale shows the LR probability of the matched optical source. Each image is 1.25 ' in diameter.

6.A Radio-Optical Matches

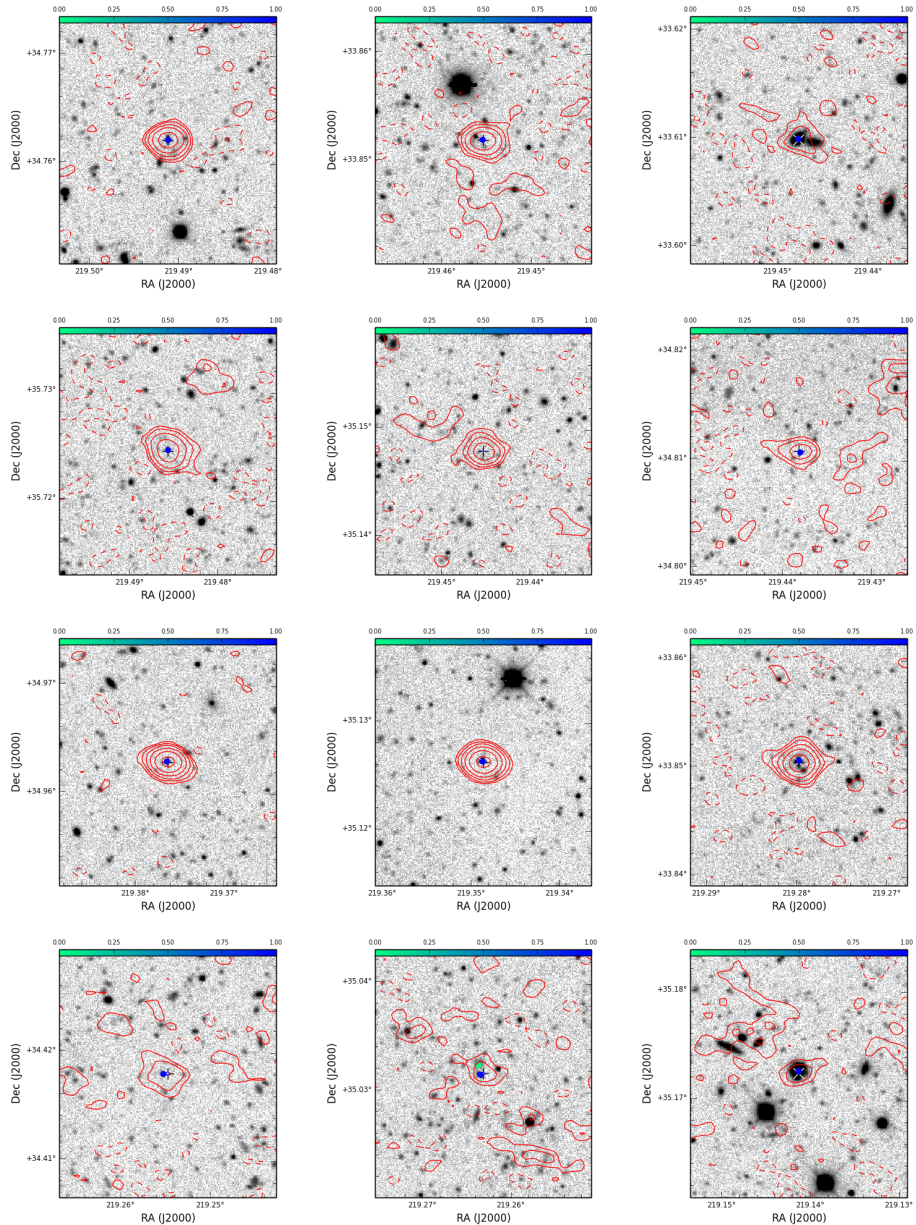


Figure 6.A.1: Cont.

6 Radio AGN in the Boötes field:

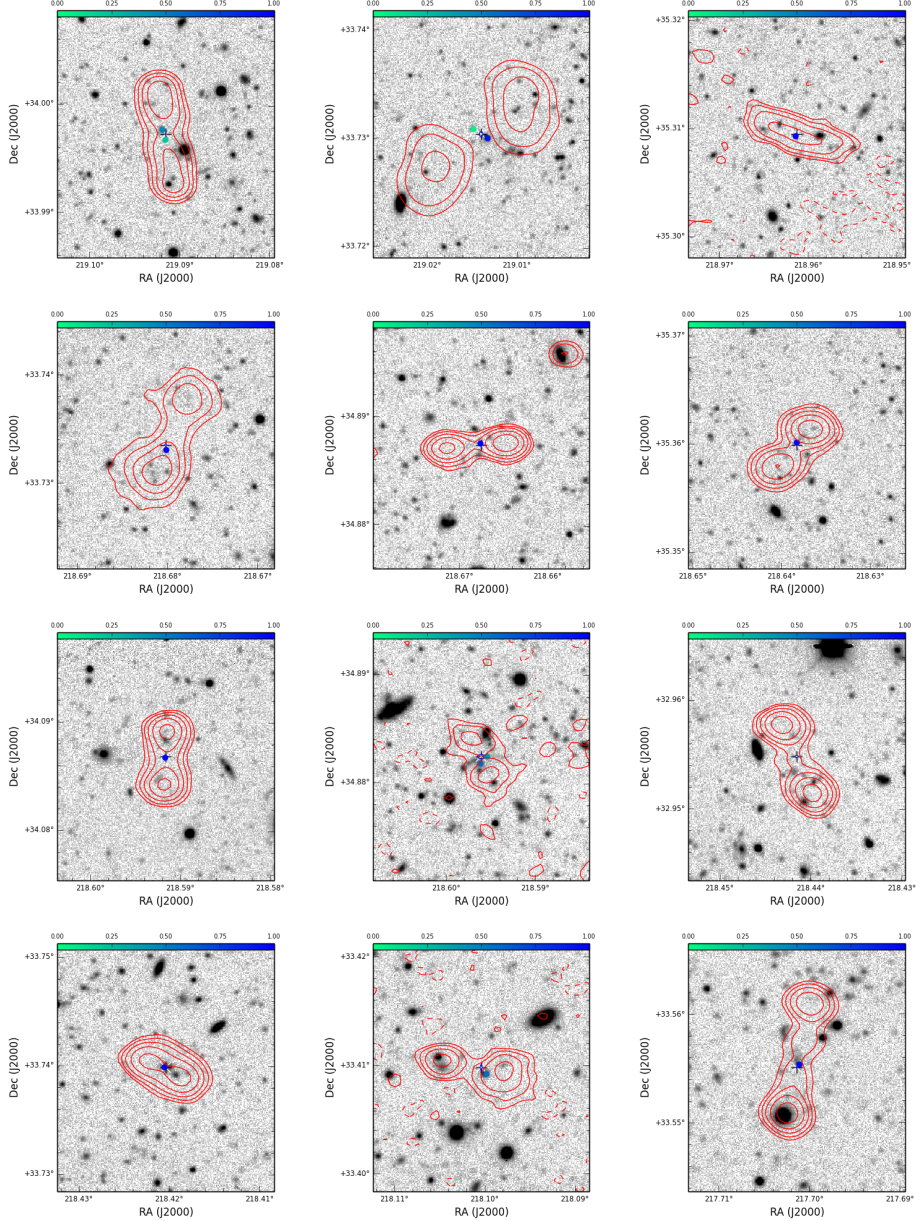


Figure 6.A.2: Examples of the radio-optical cross matches in Class 2. The greyscale image show the I -band NDWFS image. The red contours show the LOFAR 150 MHz image at levels of $3\sigma_{\text{local}} \times [1, 1.4, 2, 2.8, \dots]$ where σ_{local} is the local rms in the LOFAR map at the source position. The blue colorscale shows the LR probability of the matched optical source. Each image is 1.25 ' in diameter.

6.A Radio-Optical Matches

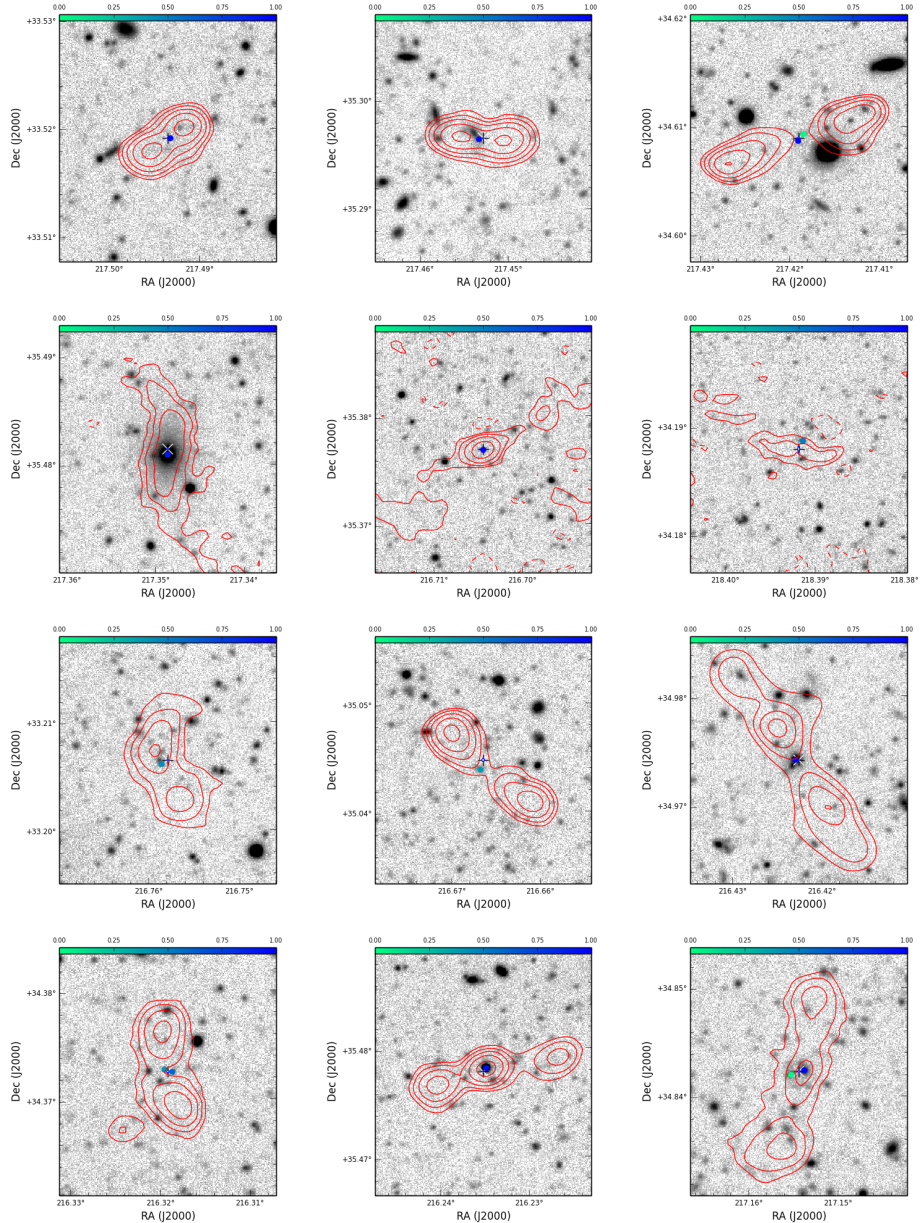


Figure 6.A.2: Cont.

6 Radio AGN in the Boötes field:

6.B Example SED fits

Some examples of the AGNFITTER SEDs with components in the three redshift intervals are shown in Fig. 6.B.1 and Fig. 6.B.2 for sources with good quality fits (quantified by likelihood values close to -1) and in Fig. 6.B.3 for sources with poor fits (quantified by likelihood values $\lesssim -20$). These include both HERGs and LERGs in each redshift interval.

6.B Example SED fits

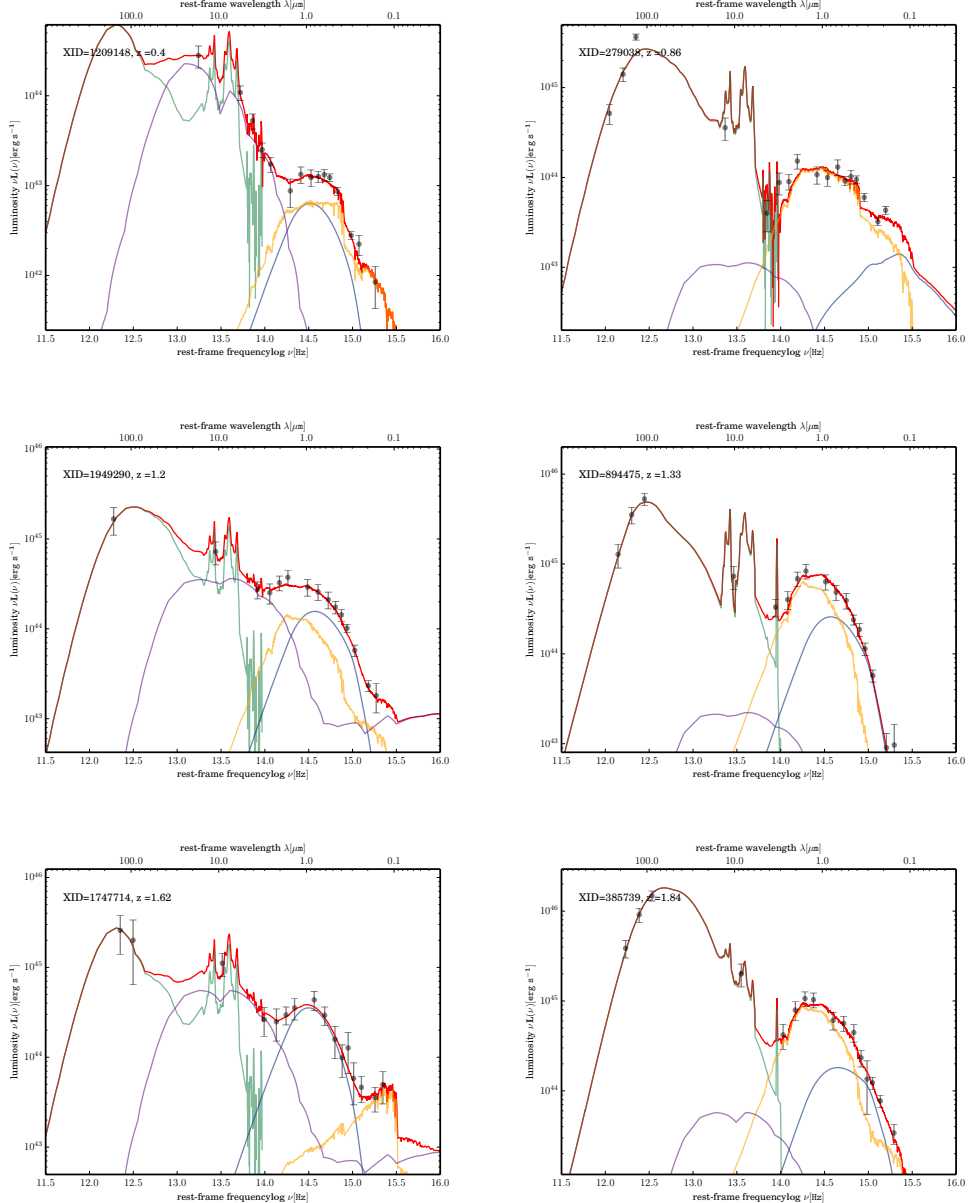


Figure 6.B.1: Examples of good quality SED Fits (with likelihood ≈ -1) with significant star formation contribution (high f_{SB} values) for *left* HERGs and *right* LERGs in the three redshift bins $0.5 < z \leq 1.0$ (*top*), $1.0 < z \leq 1.5$ (*middle*) and $1.5 < z \leq 2.0$ (*bottom*). In all cases the maximum likelihood realisation is plotted (red) and the fitted components are the AGN torus (purple), the starburst (green), the galaxy (yellow) and the blue bump (blue) with the total SED in red.

6 Radio AGN in the Boötes field:

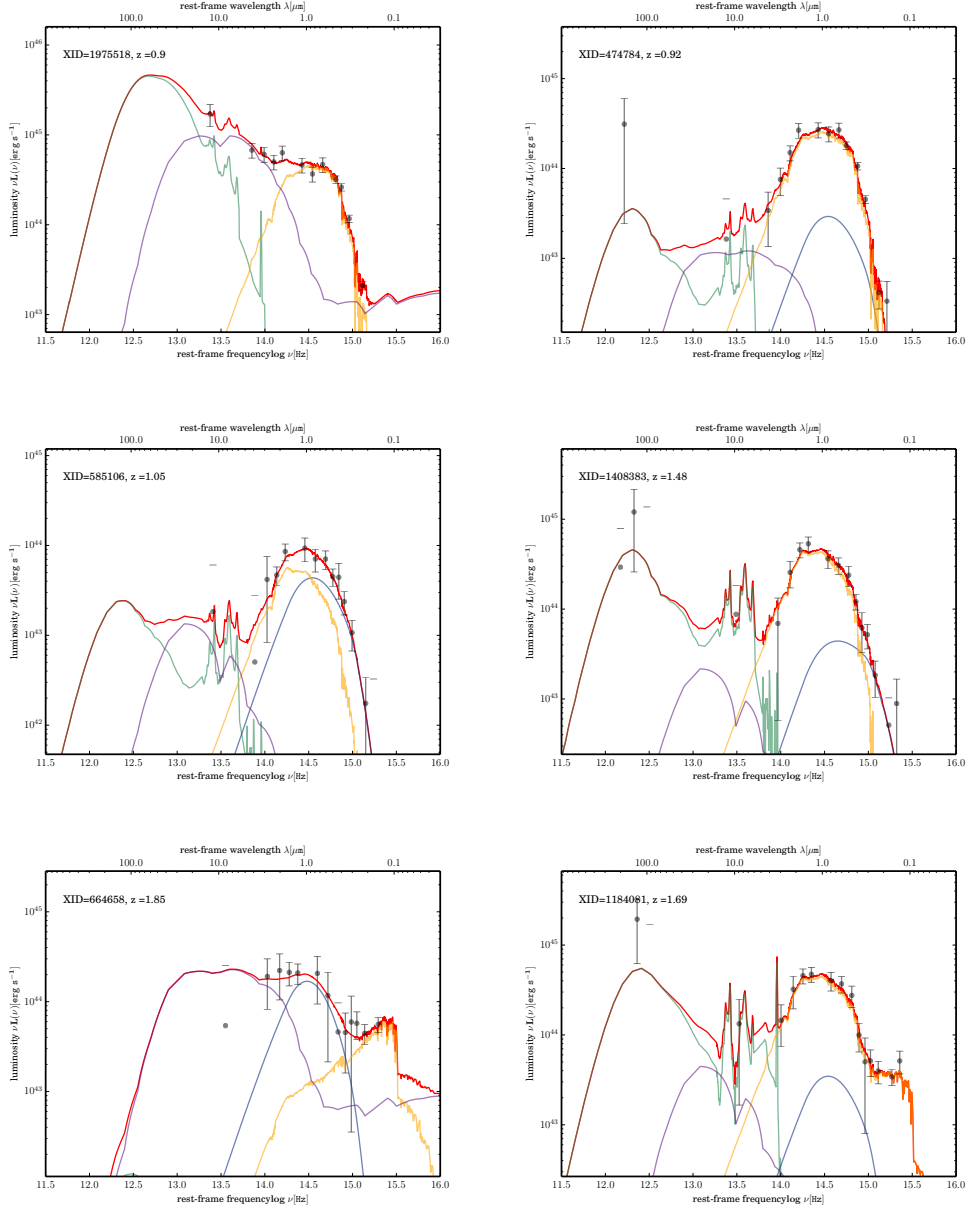


Figure 6.B.2: Examples of good quality SED Fits (with likelihood ≈ -1) with minimal star formation contribution (low f_{SB} values) for *left* HERGs and *right* LERGs in the three redshift bins $0.5 < z \leq 1.0$ (*top*), $1.0 < z \leq 1.5$ (*middle*) and $1.5 < z \leq 2.0$ (*bottom*). In all cases the maximum likelihood realisation is plotted (red) and the fitted components are the AGN torus (purple), the starburst (green), the galaxy (yellow) and the blue bump (blue) with the total SED in red.

6.B Example SED fits

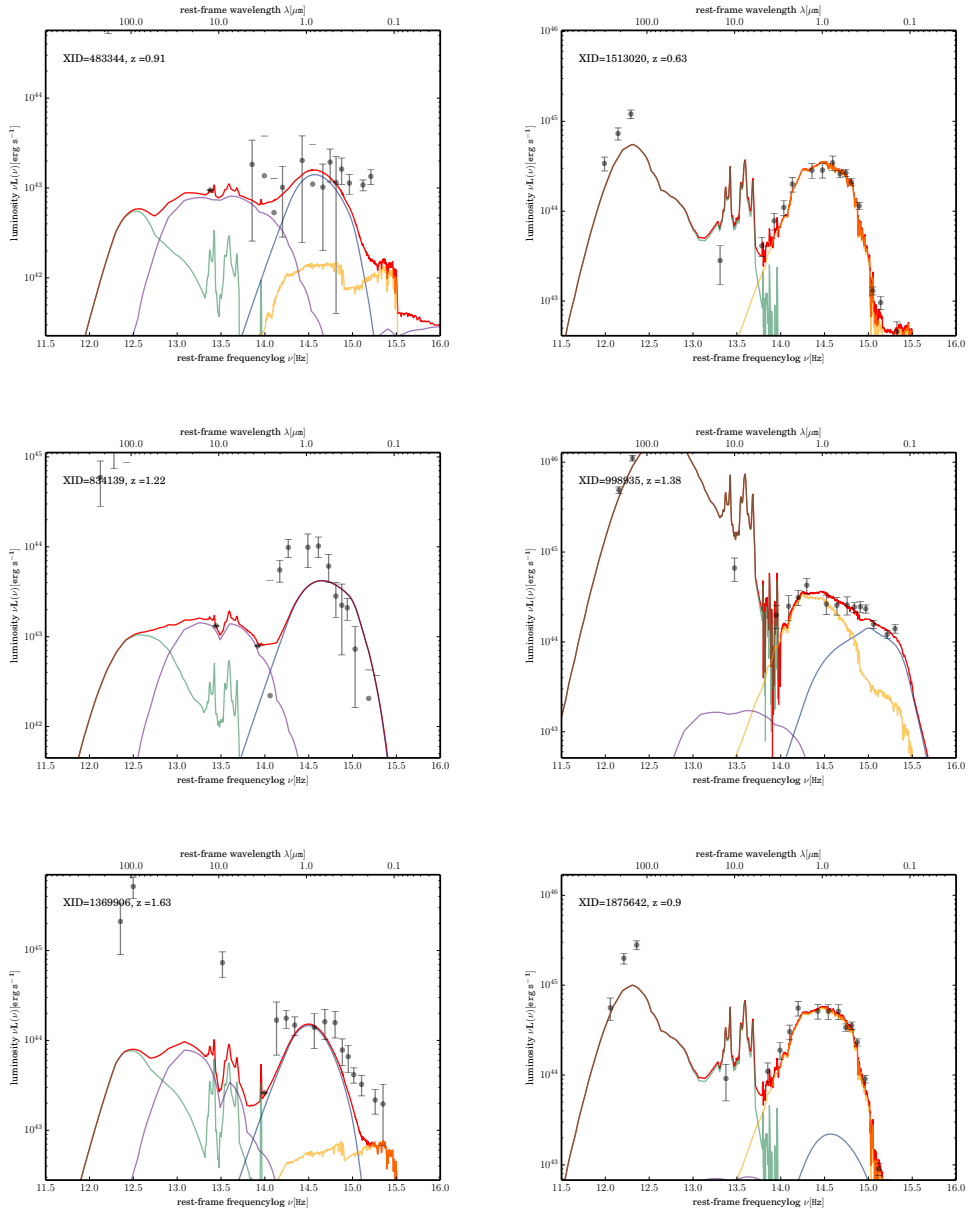


Figure 6.B.3: Examples of poorer SED Fits (with likelihood ≈ -20) for left HERGs and right LERGs in the three redshift bins $0.5 < z \leq 1.0$ (top), $1.0 < z \leq 1.5$ (middle) and $1.5 < z \leq 2.0$ (bottom). In all cases the maximum likelihood realisation is plotted (red) and the fitted components are the AGN torus (purple), the starburst (green), the galaxy (yellow) and the blue bump (blue) with the total SED in red.

6 Radio AGN in the Boötes field:

Bibliography

- Abazajian K. N., et al., 2009, ApJS, 182, 543
Antonucci R., 1993, ARA&A, 31, 473
Ashby M. L. N., et al., 2009, ApJ, 701, 428
Assef R. J., et al., 2010, ApJ, 713, 970
Autry R. G., et al., 2003, in Iye M., Moorwood A. F. M., eds, Society of Photo-Optical Instrumentation Engineers (SPIE) Conference Series Vol. 4841, Instrument Design and Performance for Optical/Infrared Ground-based Telescopes. pp 525–539, doi:10.1117/12.460419
Balogh M. L., Morris S. L., Yee H. K. C., Carlberg R. G., Ellingson E., 1999, ApJ, 527, 54
Barthel P. D., 1989, ApJ, 336, 606
Becker R. H., White R. L., Helfand D. J., 1995, ApJ, 450, 559
Benn C. R., 1983, The Observatory, 103, 150
Bertin E., Arnouts S., 1996, A&AS, 117, 393
Best P. N., Heckman T. M., 2012, MNRAS, 421, 1569
Best P. N., Arts J. N., Röttgering H. J. A., Rengelink R., Brookes M. H., Wall J., 2003, MNRAS, 346, 627
Best P. N., Kauffmann G., Heckman T. M., Ivezić Ž., 2005a, MNRAS, 362, 9
Best P. N., Kauffmann G., Heckman T. M., Brinchmann J., Charlot S., Ivezić Ž., White S. D. M., 2005b, MNRAS, 362, 25
Best P. N., Kaiser C. R., Heckman T. M., Kauffmann G., 2006, MNRAS, 368, L67
Best P. N., von der Linden A., Kauffmann G., Heckman T. M., Kaiser C. R., 2007, MNRAS, 379, 894
Best P. N., Ker L. M., Simpson C., Rigby E. E., Sabater J., 2014, MNRAS, 445, 955
Bian F., et al., 2013, ApJ, 774, 28
Bianchi L., Conti A., Shiao B., 2014, Advances in Space Research, 53, 900
Blanton M. R., et al., 2003a, AJ, 125, 2348
Blanton M. R., et al., 2003b, ApJ, 592, 819
Blanton M. R., et al., 2003c, ApJ, 594, 186
Bower R. G., Benson A. J., Malbon R., Helly J. C., Frenk C. S., Baugh C. M., Cole S., Lacey C. G., 2006, MNRAS, 370, 645
Brammer G. B., van Dokkum P. G., Coppi P., 2008, ApJ, 686, 1503
Brand K., et al., 2006, ApJ, 641, 140
Brinchmann J., Charlot S., White S. D. M., Tremonti C., Kauffmann G., Heckman T., Brinkmann J., 2004, MNRAS, 351, 1151
Brodwin M., et al., 2006, ApJ, 651, 791
Brown M. J. I., Dey A., Jannuzzi B. T., Brand K., Benson A. J., Brodwin M., Croton D. J., Eisenhardt P. R., 2007, ApJ, 654, 858
Brown M. J. I., et al., 2008, ApJ, 682, 937
Brown M. J. I., et al., 2014, ApJS, 212, 18
Bruzual G., Charlot S., 2003, MNRAS, 344, 1000
Calistro Rivera G., Lusso E., Hennawi J. H., Hogg D. W., 2015

Bibliography

- Calzetti D., Armus L., Bohlin R. C., Kinney A. L., Koornneef J., Storchi-Bergmann T., 2000, ApJ, 533, 682
- Cattaneo A., et al., 2009, Nature, 460, 213
- Chabrier G., 2003, PASP, 115, 763
- Condon J. J., 1989, ApJ, 338, 13
- Condon J. J., 1992, ARA&A, 30, 575
- Condon J. J., Cotton W. D., Greisen E. W., Yin Q. F., Perley R. A., Taylor G. B., Broderick J. J., 1998, AJ, 115, 1693
- Cool R. J., 2007, ApJS, 169, 21
- Cool R. J., et al., 2012, ApJ, 748, 10
- Croton D. J., et al., 2006, MNRAS, 365, 11
- Donley J. L., et al., 2012, ApJ, 748, 142
- Eales S., Rawlings S., Law-Green D., Cotter G., Lacy M., 1997, MNRAS, 291, 593
- Evans D. A., Worrall D. M., Hardcastle M. J., Kraft R. P., Birkishaw M., 2006, ApJ, 642, 96
- Fabian A. C., Celotti A., Erlund M. C., 2006, MNRAS, 373, L16
- Fabricant D., et al., 2005, PASP, 117, 1411
- Fanaroff B. L., Riley J. M., 1974, MNRAS, 167, 31P
- Fernandes C. A. C., et al., 2015, MNRAS, 447, 1184
- Griffin M. J., et al., 2010, A&A, 518, L3
- Gürkan G., Hardcastle M. J., Jarvis M. J., 2014, MNRAS, 438, 1149
- Hardcastle M. J., Evans D. A., Croston J. H., 2006, MNRAS, 370, 1893
- Hardcastle M. J., Evans D. A., Croston J. H., 2007, MNRAS, 376, 1849
- Heckman T. M., Best P. N., 2014, ARA&A, 52, 589
- Hickox R. C., et al., 2009, ApJ, 696, 891
- Hine R. G., Longair M. S., 1979, MNRAS, 188, 111
- Ilbert O., et al., 2009, ApJ, 690, 1236
- Jackson N., Rawlings S., 1997, MNRAS, 286, 241
- Jannuzzi B. T., Dey A., NDWFS Team 1999, in American Astronomical Society Meeting Abstracts. p. 1392
- Jannuzzi B., et al., 2010, in American Astronomical Society Meeting Abstracts #215. p. 470.01
- Janssen R. M. J., Röttgering H. J. A., Best P. N., Brinchmann J., 2012, A&A, 541, A62
- Jarvis M. J., et al., 2001, MNRAS, 326, 1563
- Kauffmann G., et al., 2003, MNRAS, 341, 33
- Kenter A., et al., 2005, ApJS, 161, 9
- Kochanek C. S., et al., 2012, ApJS, 200, 8
- Kriek M., van Dokkum P. G., Labbé I., Franx M., Illingworth G. D., Marchesini D., Quadri R. F., 2009, ApJ, 700, 221
- Laing R. A., Jenkins C. R., Wall J. V., Unger S. W., 1994, in Bicknell G. V., Dopita M. A., Quinn P. J., eds, Astronomical Society of the Pacific Conference Series Vol. 54, The Physics of Active Galaxies. p. 201
- Magorrian J., et al., 1998, AJ, 115, 2285
- Martin C., et al., 2003, in Blades J. C., Siegmund O. H. W., eds, Society of Photo-Optical Instrumentation Engineers (SPIE) Conference Series Vol. 4854, Future EUV/UV and Visible Space Astrophysics Missions and Instrumentation.. pp 336–350, doi:10.1117/12.460034
- McNamara B. R., Nulsen P. E. J., 2012, New Journal of Physics, 14, 055023
- Mingo B., Hardcastle M. J., Croston J. H., Dicken D., Evans D. A., Morganti R., Tadhunter C., 2014, MNRAS, 440, 269

Bibliography

- Murray S. S., et al., 2005, ApJS, 161, 1
Muzzin A., et al., 2013, ApJS, 206, 8
Narayan R., Yi I., 1995, ApJ, 452, 710
Ogle P., Whysong D., Antonucci R., 2006, ApJ, 647, 161
Oliver S. J., et al., 2012, MNRAS, 424, 1614
Prestage R. M., Peacock J. A., 1983, MNRAS, 204, 355
Richter G. A., 1975, Astronomische Nachrichten, 296, 65
Rigby E. E., et al., 2015
Roseboom I. G., et al., 2010, MNRAS, 409, 48
Rowan-Robinson M., et al., 2008, MNRAS, 386, 697
Russell H. R., McNamara B. R., Edge A. C., Hogan M. T., Main R. A., Vantyghem A. N., 2013, MNRAS, 432, 530
Salvato M., et al., 2009, ApJ, 690, 1250
Salvato M., et al., 2011, ApJ, 742, 61
Schmidt M., 1968, ApJ, 151, 393
Seymour N., et al., 2007, ApJS, 171, 353
Shakura N. I., Sunyaev R. A., 1973, A&A, 24, 337
Silk J., Rees M. J., 1998, A&A, 331, L1
Son D., Woo J.-H., Kim S. C., Fu H., Kawakatu N., Bennert V. N., Nagao T., Park D., 2012, ApJ, 757, 140
Stern D., et al., 2005, ApJ, 631, 163
Stern D., et al., 2012, ApJ, 753, 30
Sutherland W., Saunders W., 1992, MNRAS, 259, 413
Tasse C., Le Borgne D., Röttgering H., Best P. N., Pierre M., Rocca-Volmerange B., 2008a, A&A, 490, 879
Tasse C., Best P. N., Röttgering H., Le Borgne D., 2008b, A&A, 490, 893
Taylor E. N., et al., 2009, ApJS, 183, 295
Taylor E. N., et al., 2011, MNRAS, 418, 1587
Urry C. M., Padovani P., 1995, PASP, 107, 803
Whysong D., Antonucci R., 2004, ApJ, 602, 116
Williams W. L., Röttgering H. J. A., 2015, MNRAS, 450, 1538
Williams W. L., et al., 2015
Wolstencroft R. D., Savage A., Clowes R. G., MacGillivray H. T., Leggett S. K., Kalafi M., 1986, MNRAS, 223, 279
York D. G., et al., 2000, AJ, 120, 1579
de Vries W. H., Morganti R., Röttgering H. J. A., Vermeulen R., van Breugel W., Rengelink R., Jarvis M. J., 2002, AJ, 123, 1784
van Haarlem M. P., et al., 2013, A&A, 556, A2
van Weeren R. J., in prep.

Bibliography